Schweizerischer Erdbebendienst
Service Sismologique Suisse
Servizio Sismico Svizzero
Swiss Seismological Service

ETH zürich

SITE CHARACTERIZATION REPORT
SGWS: Grindelwald (BE), Schwimmbad

Agostiny Marrios Lontsi, Manuel Hobiger, Donat Fäh

Last Modification: 20th August, 2022

Schweizerischer Erdbebendienst (SED)
Service Sismologique Suisse
Servizio Sismico Svizzero
Servizi da Terratrembels Svizzer

ETH Zürich
Sonneggstrasse 5
8092 Zürich
Schweiz
agostiny.lontsi@sed.ethz.ch

Contents

Summary

A passive seismic survey was conducted at the strong-motion station SGWS in Grindelwald (BE) to characterize the underlying subsurface. The geophysical site characterization aims at using ambient seismic vibration recordings to infer the shear-wave velocity profile around the installed seismological station.
The horizontal-to-vertical (H/V) spectral ratio analysis for a temporary velocitimeter station deployed next to SGWS shows two peaks at 1.1-, and 25.7 Hz with amplitudes of 3.0, and 4.1, respectively.
The array methods used include spatial autocorrelation, 3-C high-resolution frequency-wavenumber, wavefield decomposition, and interferometric multichannel analysis of surface waves. Within the array resolution limits, they provide clear and broad phase velocity dispersion curves for Rayleigh and Love waves in the frequency range between 1.7 and 20.3 Hz. Two Rayleigh wave branches are observed within this frequency band and interpreted as fundamental and first higher modes, respectively. One Love wave branch is observed and interpreted as fundamental mode.
Two combined inversions are performed, one inverting the fundamental mode ellipticity and dispersion curves, and the second inverting the full H/V and dispersion curves. The first inversion indicates three major shear-wave velocity discontinuities at around 1.0-, 10.0-, and 400.0 m depth and the second inversion indicates a shear-wave velocity discontinuities at around 2.8 m and 125.0 m depth. The average V_{S30} are 525 ± 2 m/s and 588 ± 2 m/s for the first and second inversion, respectively. This V_{S30} value corresponds to ground type B in both EC8 (European standard) and SIA261 (Swiss standard). These bedrock depth and V_{S30} values variations are reflected on the modelled theoretical SH-wave transfer function. In both cases, the SH-wave transfer function is compared with the empirical amplification function obtained from earthquake observations.

1 Introduction

As part of the second phase of the Swiss Strong Motion Network renewal project, a strong motion station was built by the area of the public Swimming pool in Grindelwald (BE). The station SGWS went operational on October 2nd, 2019. At this site, a passive seismic survey was performed to record the propagating ambient noise wavefield. We use single-station and array methods to analyze the dispersion characteristics of Rayleigh and Love waves in the recorded noise wavefields. In a first inversion, the estimated fundamental mode ellipticity branches and the phase velocity dispersion information are combined to infer the underlying subsurface structure and the corresponding 1D shear wave velocity information (e.g. Scherbaum et al. 2003; Hobiger et al. 2013). In a second inversion, the full H/V curve and the interpreted phase velocity dispersion information are combined to obtain the shear-wave velocity profile (Lontsi et al., 2016b).

2 Site and geological setting

Figure 1 shows the location of Grindelwald in Switzerland and the surface geology at the array sites. Most of the stations sit on moraine.

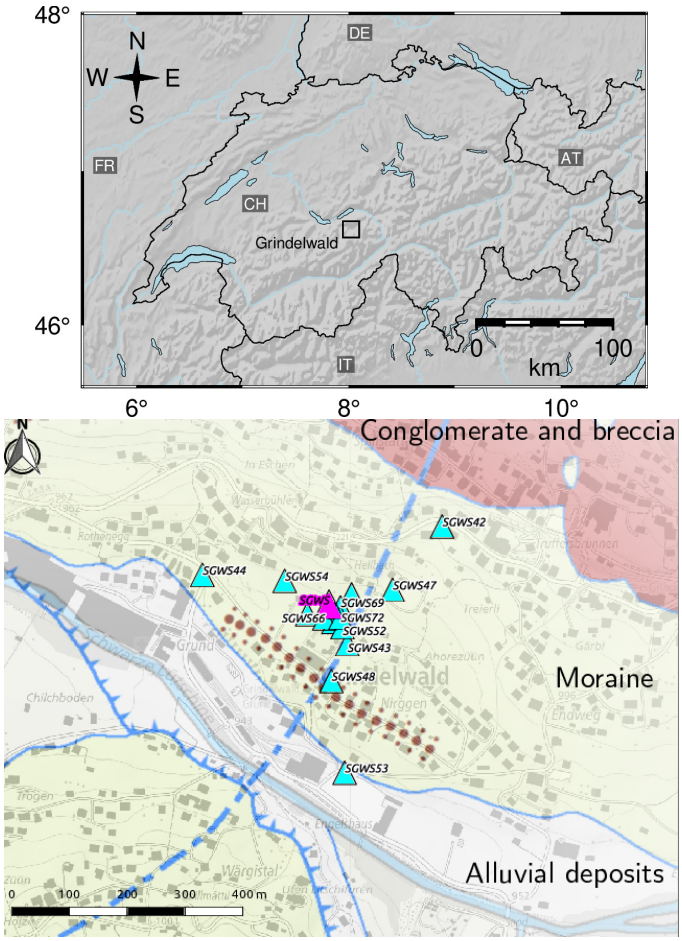

Figure 1: Top: Location of the strong motion station in Grindelwald (BE). Bottom: The strong motion station SGWS and the array geometry on top of the surface geology for the measurement site.

3 Overview of the site characterization measurement

In order to characterize the local underground structure around station SGWS, a passive seismic array measurement was carried out on November 6^{th}, 2020. Figure 2 shows an aerial image of the survey site, indicating the permanent station SGWS (purple triangle) and the temporary array deployment (white triangles) for ambient noise measurements. The array consisted of 16 stations. It was planned to have five rings of three stations each around a central station. The minimum and maximum inter-station distances of the final array layout were 8.0 and 461.5 m, respectively. The seismic stations consisted of Lennartz 3C 5 s sensors connected to Centaur digitizers. A total of 12 digitizers were used. Twelve sensors were connected to the A channels of the digitizers and another four sensors were connected to the B channels. The sampling rate was 200 Hz. The stations of the temporary array are named by adding a two-digit number to the permanent station name. The two-digit numbers are directly related to the last two digits of the recorder serial numbers for stations connected to channel A and augmented by 20 for stations connected to channel B. The array continuously recorded ambient vibrations for 2h between 12:59 and 14:59 (UTC).
The station locations have been measured by a differential GPS system (Leica Viva GS10) which was set up to measure with a precision better than 5 cm. This precision was achieved at all stations, with a maximum uncertainty of 3.2 cm.

Figure 2: Aerial image of the survey site at Grindelwald with the strong motion station location and array configuration. Source of the aerial map: Federal Office of Topography.

4 Single-station analysis

4.1 Microtremor H/V and ellipticity estimation

The microtremor H/V spectral ratio and the ellipticity curves are obtained using 6 different techniques:

- geopsyhv: full microtremor H/V estimation (www.geopsy.org);
- RayDec, optimized for Rayleigh wave ellipticity estimation (Hobiger et al., 2009);
- FTAN, optimized for Rayleigh wave ellipticity estimation (Fäh et al., 2009);
- CLASS, optimized for Rayleigh wave ellipticity estimation (Fäh et al., 2001);
- VPTFA, optimized for Rayleigh wave ellipticity estimation (Poggi & Fäh, 2010);
- MTSPEC, optimized for Rayleigh wave ellipticity estimation (Burjánek et al., 2010).

The H/V and Rayleigh wave ellipticity results for each station using the 6 techniques are shown in Figure 3 for comparison. The spatial variability of the H/V spectral ratio within the array is highlighted by showing the H/V spectral ratio curves on the aerial map (Figure 4).
At each station, two peak frequencies are observed and picked in the frequency range between 0.2 and 20.0 Hz (Figure 5). The first peak frequency is at about 1.1 Hz and shows a little spread. The second peak frequency is observed above 5 Hz and shows a wide spread among stations. The station SGWS55 is particularly characterized by a lower peak frequency at 0.33 Hz. This can be undestood by the bad coupling between the sensor and the ground. After deployment, we latter observed water in the sensor hole. Above 20 Hz, some stations present an additional peak on the H/V spectral ratio curves (see Figure 3).

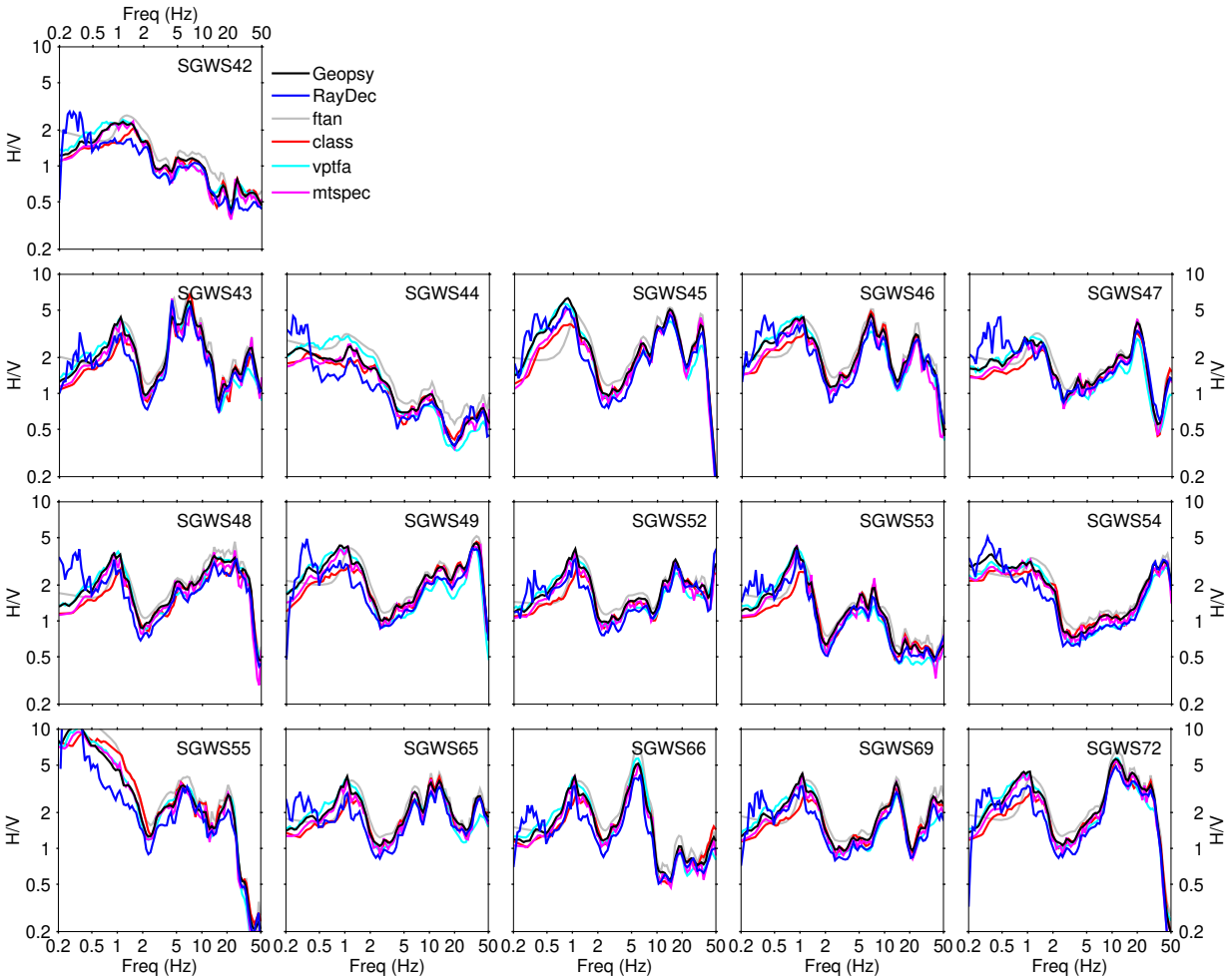

Figure 3: Ellipticity and H/V spectral ratio estimation using different techniques.

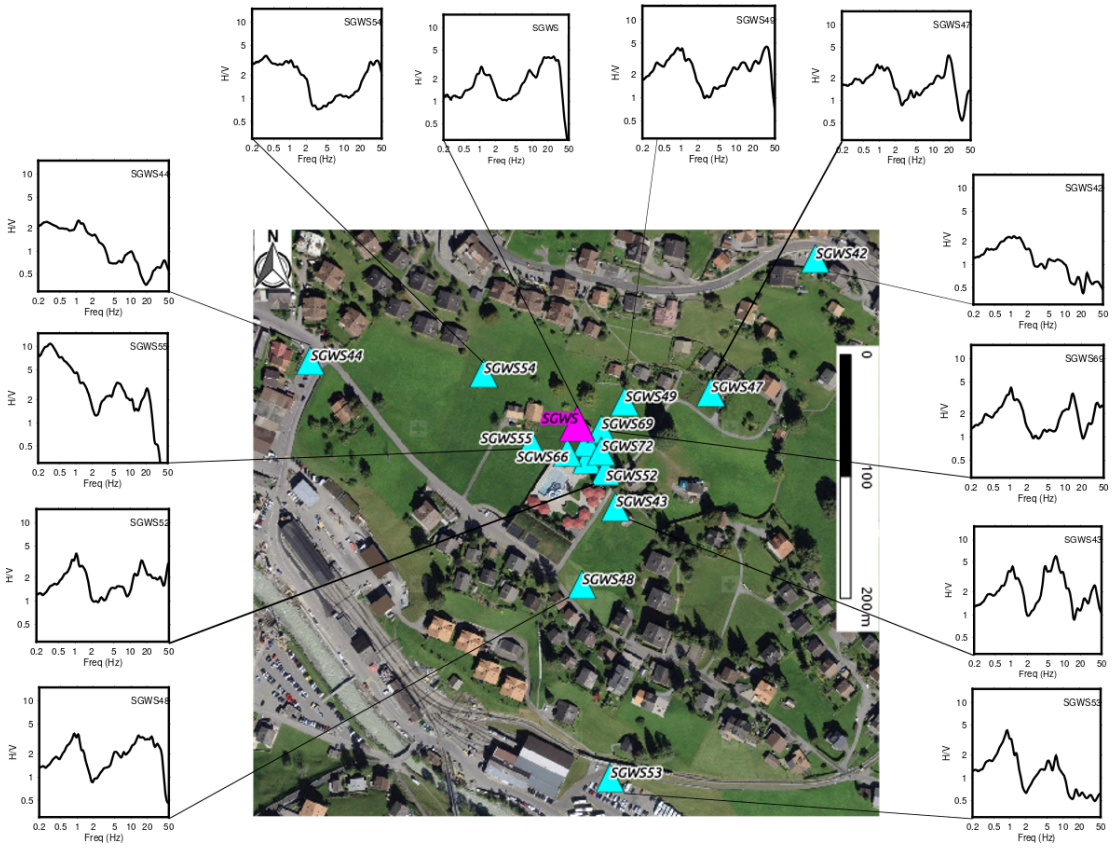

Figure 4: H/V spatial variability around the strong motion station at Grindelwald.

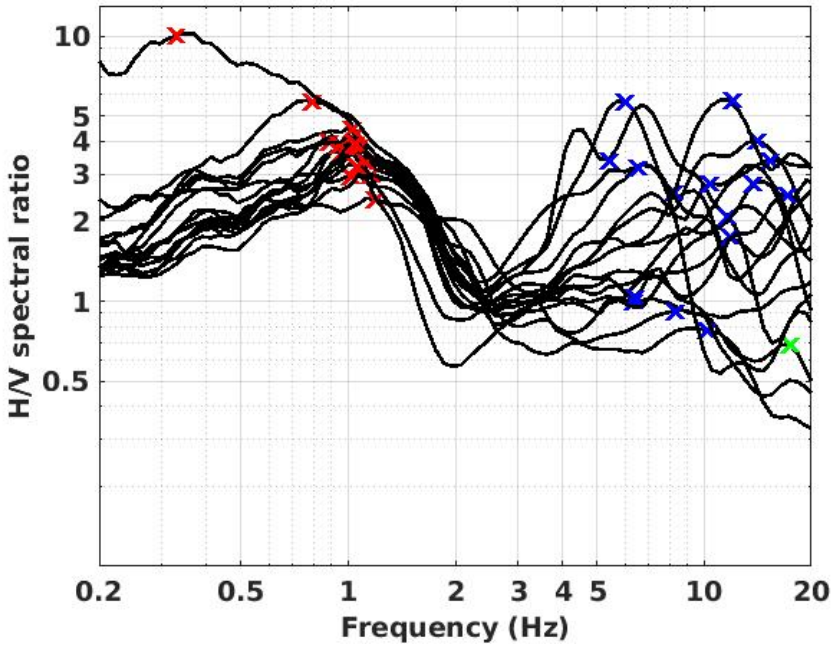

Figure 5: Overview of the H/V curves of the different stations, obtained using the ellipticity technique by Poggi & Fäh (2010); see also *vptfa* in Figure 3. For the presented frequency range (0.2 - 20 Hz), the red and blue markers indicate the frequencies of the first and second maxima in the H/V spectral ratio curves, respectively.

4.2 Polarization analysis

Following Burjánek et al. (2010, 2012), the polarization analysis is performed to assess potential 2D effects. The results are shown in Figure 6 for station SGWS69, that is located close to SGWS.
The analysis indicates no preferential polarization except for a slight indication of polarized particle motion around 1.1 Hz, where the low ellipticity value indicates a predominantly linear particle motion. This is in agreement with the strong H/V and Rayleigh wave ellipticity values at this frequency. This linear polarization is related with a weak NW-SE strike direction, in the direction along the valley. Weak SW-NE and N-S strike directions can also be at 4 Hz and 14 Hz, respectively.

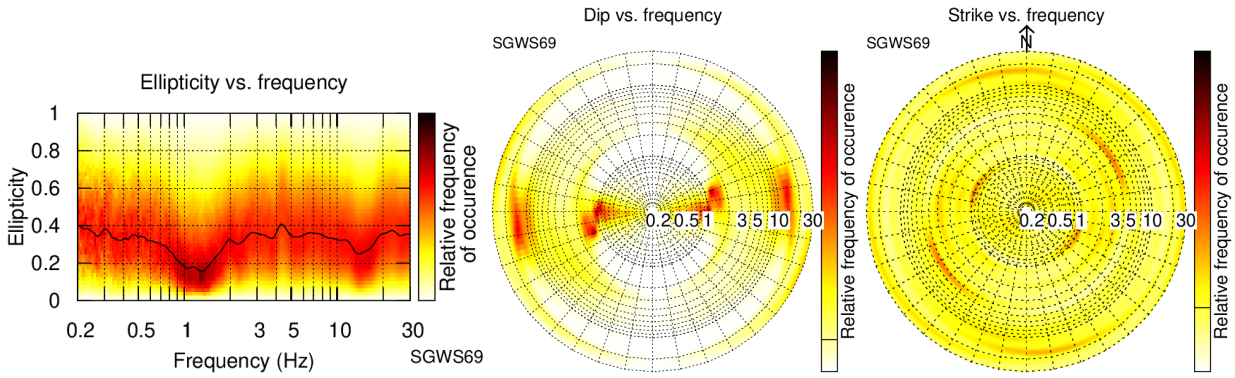

Figure 6: Polarization analysis for station SGWS69, located next to the permanent station.

5 Array analysis

The phase velocities for Rayleigh and Love waves are estimated for the full array of 16 stations using four different array methods:

1. Spatial autocorrelation (SPAC, Aki 1957; Bettig et al. 2001);
2. High resolution frequency-wavenumber (HRFK, Poggi & Fäh 2010);
3. Wavefield decomposition (WaveDec, Maranò et al. 2012);
4. Interferometric Multichannel Analysis of Surface Waves (IMASW, Lontsi et al. 2016a).

5.1 SPAC

The SPAC (Aki, 1957) curves of the vertical components have been calculated using the M-SPAC (Bettig et al., 2001) technique implemented in geopsy. Rings with different radius ranges are defined and for all station pairs with distance inside this radius range, the cross-correlation is calculated over a wide frequency range. These cross-correlation curves are averaged for all station pairs of the respective ring and give the SPAC curves. The cross-correlation curves for all SPAC rings are shown in Figure 7. The phase velocity is obtained through a non-linear inversion of the estimated autocorrelation coefficients. This is made with the function spac2disp of the geopsy package. Using SPAC, we can retrieve a Rayleigh wave phase-velocity dispersion curve between 2 and 4 Hz.

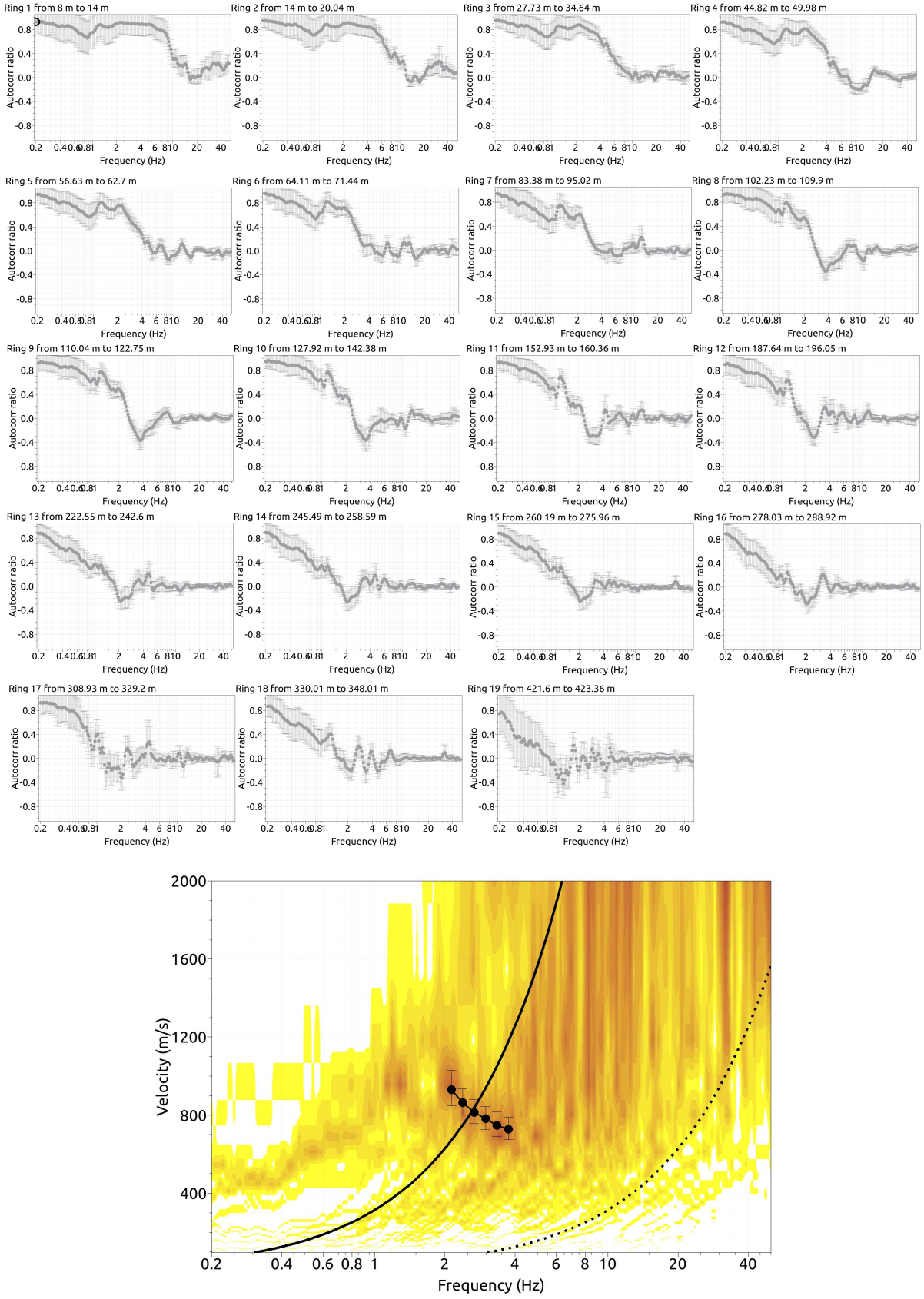

Figure 7: Top: M-SPAC results for the different rings. Bottom: Dispersion curve map with a clear dispersion curve branch between 2 and 4 Hz.

5.2 HRFK

Figure 8 shows the dispersion characteristic for Love waves on the transverse component and that of Rayleigh waves on the radial and vertical components. We identified and picked one branch for the Love waves on the transverse component and one branch for Rayleigh waves on the radial and vertical components. The mode number was attributed after the results of all array methods were put together.

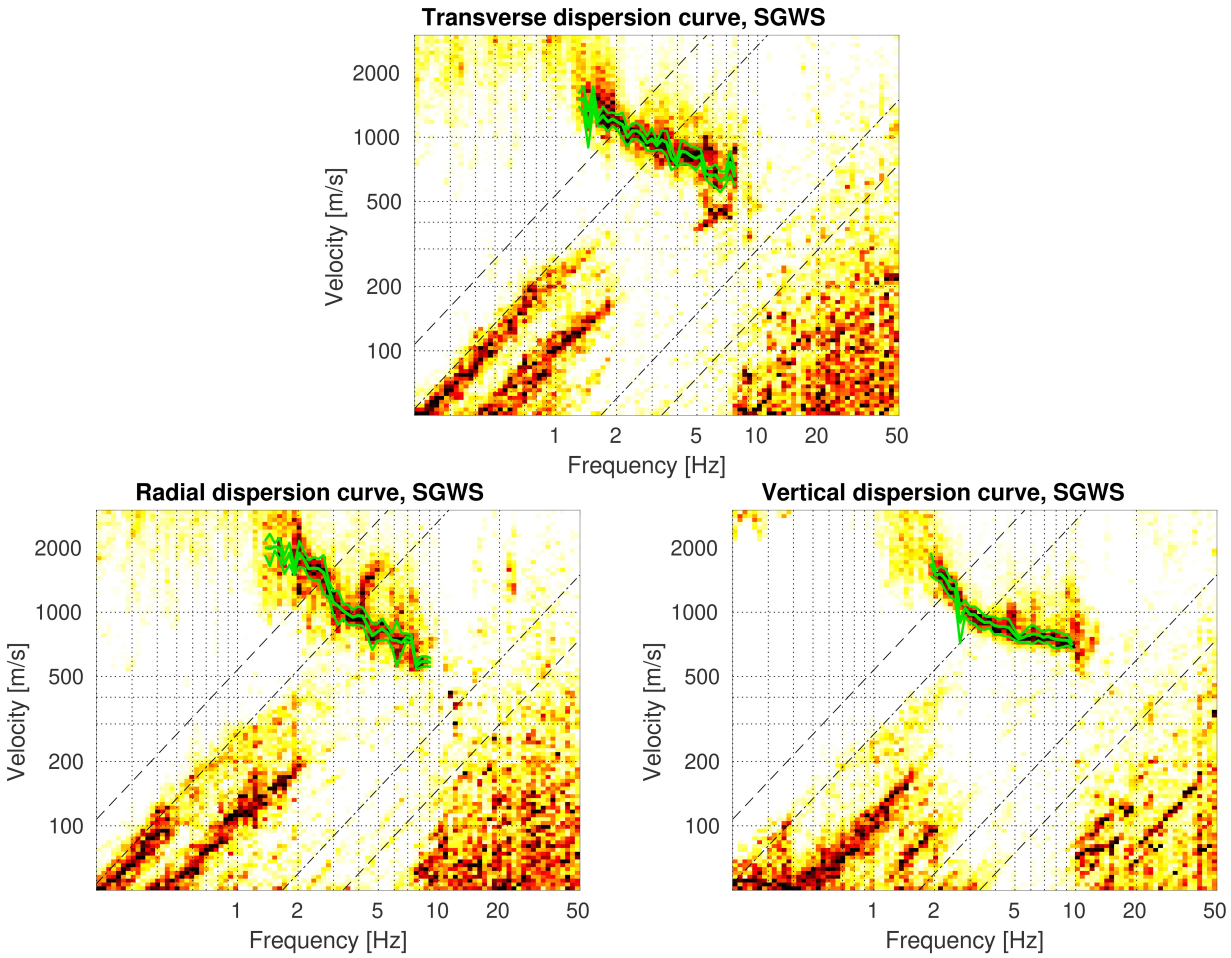

Figure 8: HRFK results. The phase velocity dispersion curves on the three components are shown. The phase velocity dispersion branches are picked on the transverse component for Love waves and on the vertical and radial components for Rayleigh waves. The dashed and dotted black lines are the array resolution limits. The solid green curves are picked from the data, where the central line indicates the best values and the two outer curves the standard deviation.

5.3 WaveDec

The WaveDec results are shown in Figure 9. We observe and pick one phase velocity dispersion branch for the Rayleigh and one branch for the Love waves. The ellipticity curve was picked in the frequency range of the Rayleigh wave dispersion curve and shows a retrograde particle motion.

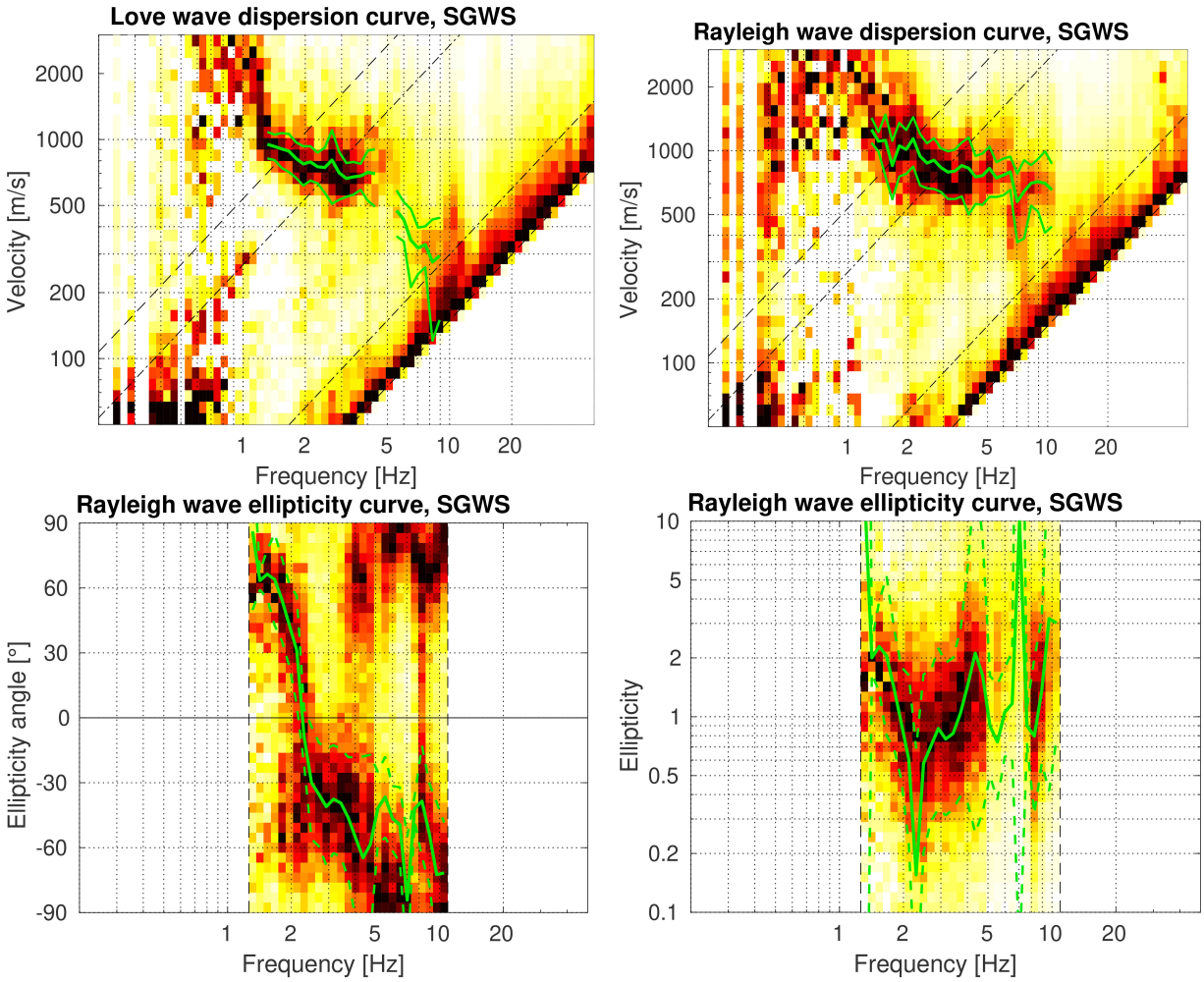

Figure 9: WaveDec results: ellipticity and phase velocity dispersion curves for Rayleigh and Love waves. The phase velocity dispersion branches are picked within the array resolution limits. The solid green curves are picked from the data, where the central line indicates the best values and the two outer curves the standard deviation.

5.4 Interferometric-Multichannel Analysis of Surface Waves (IMASW)

For the IMASW analysis, the correlation functions with 100 m maximum inter-station distance are used. For this maximum inter-station distance, a clear propagation of Rayleigh waves for the vertical component can be observed. Figure 10 shows the cross-correlation results and the resulting dispersion curve map. The dispersion characteristic of the Rayleigh waves is identified and manually picked.

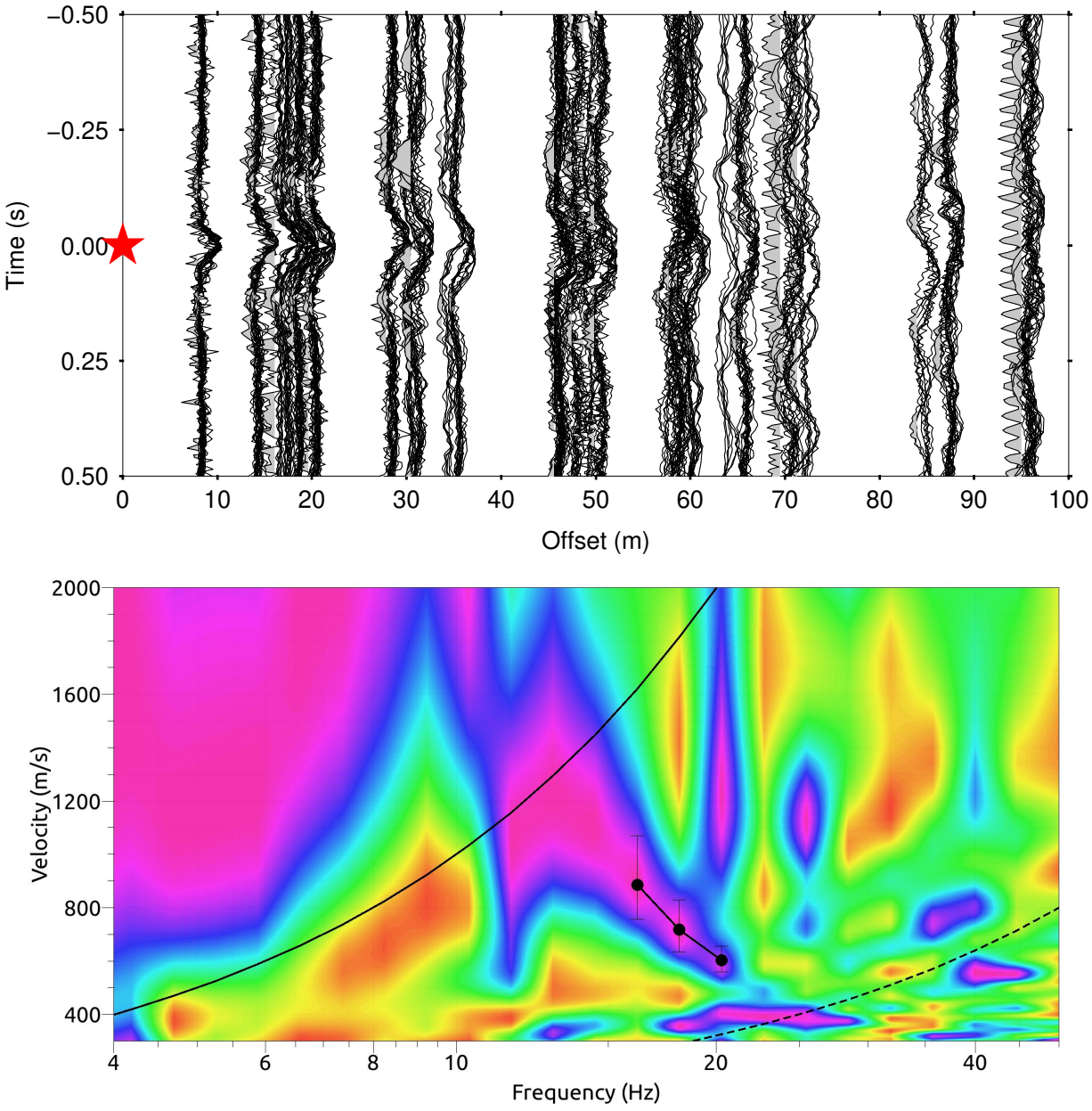

Figure 10: Top: Resulting cross-correlation Green's functions from receiver pair combinations with a maximum inter-station distance of 100 m (See array setup in Figure 2). The traces are unfiltered. The red star represents the virtual source. Bottom: frequency-wavenumber results from the cross-correlation functions. A clear phase velocity dispersion curve is observed in the frequency range between 16 and 20 Hz. The continuous and dashed lines define the resolution limits.

5.5 Overview and discussion of the measurement results

A summary of the estimated H/V, ellipticity, and phase velocity dispersion curve branches using the SPAC, HRFK, WaveDec, and IMASW methods is presented in Figure 11.

The Rayleigh wave phase-velocity dispersion branches are put together and we interpret the branch from WaveDec and IMASW as fundamental and first higher mode, respectively. The Love wave phase-velocity dispersion curve from the WaveDec and HRFK are interpreted as fundamental and first higher mode, respectively. The minimum interpreted frequency for the phase velocity is 1.7 Hz. Below this value, the energy on the vertical component is vanishing as shown by the peak frequency on the H/V around 1.1 Hz. For the inversion, the left and right flanks around the peak at 25.7 Hz are used.

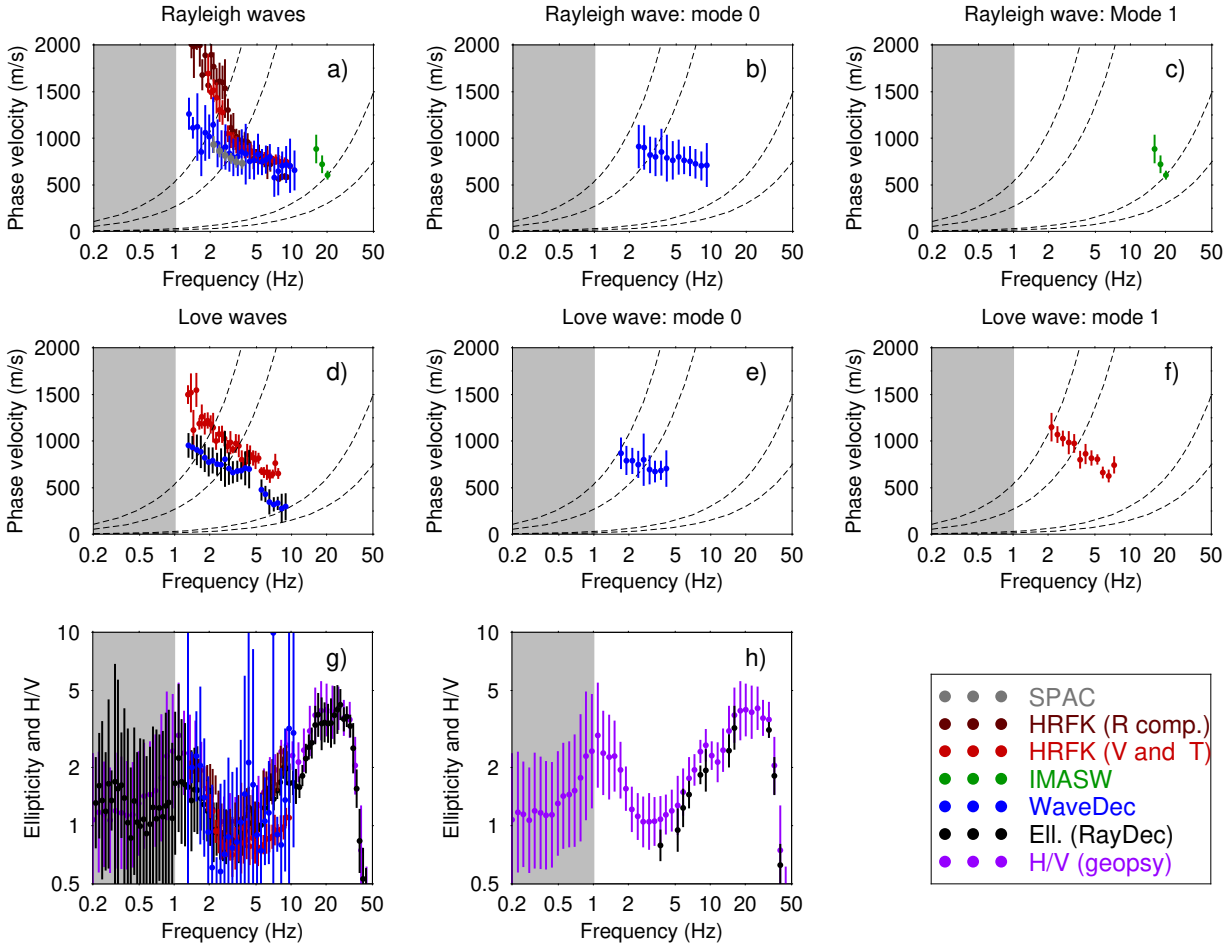

Figure 11: Overview of the results and interpreted curves obtained using the different analysis methods. a) Estimated Rayleigh wave dispersion curves. b) Interpreted Rayleigh wave phase velocity fundamental mode. c) Interpreted Rayleigh wave phase velocity first higher mode. d) Estimated Love wave dispersion curves. e) Interpreted Love wave phase velocity fundamental mode. f) Interpreted Love wave phase velocity first higher mode. g) Estimated microtremor H/V spectral ratio and Rayleigh wave ellipticity. h) Black dots indicate the fundamental mode ellipticity branches that were used in the inversion. Purple dots indicate the microtremor H/V spectral ratio used in the full-HV inversion. The gray box (see a-g) indicates additional frequency points from the ellipticity or H/V that are not covered by the dispersion curve. This additional information is useful in the inversion for constraining the bedrock depth and velocity.

6 Joint inversion of dispersion and ellipticity curves

6.1 Parametrization

The inversion assumes a layered earth structure. Three, four, five, six and seven layers over half-space were used, as well as a parameter space with fixed depths. The fixed-layer depth model consisted of 24 layers over half-space and the overall sediment cover was mostly set not to exceed 1000 m. The inversion target for the ellipticity was selected to consider the left and right flanks around the peak frequency at 25.7 Hz. The peak at 1.1 Hz was used in the inversion as an additional constrain. The inversion uses the global search neighborhood algorithm (Sambridge, 1999; Wathelet, 2008). The process is started with a set of 50 models. In each iteration step, 50 new models are generated and the 50 best models are kept for further analysis. The process is iterated a large number of times. This results here in at least 50000 generated models. The choice of the parameters for the neighborhood algorithm ensures that we sufficiently explore and exploit the parameter space. The inversion process was repeated 20 times with different seeds and the inversion with the lowest minimum misfit was retained.

6.2 Inversion results

Figures 12-17 show the combined ellipticity and phase velocity dispersion curve inversion results. We summarize and interpret the best profiles from this inversion in Figure 18. Table 1 gives a summary of the minimum misfit values achieved in each inversion process.

Table 1: Minimum misfit values for different parametrizations.

Parametrization	Minimum misfit
3 LOH	0.537
4 LOH	0.473
5 LOH	0.486
6 LOH	0.479
7 LOH	0.498
Fixed layer depth	0.522

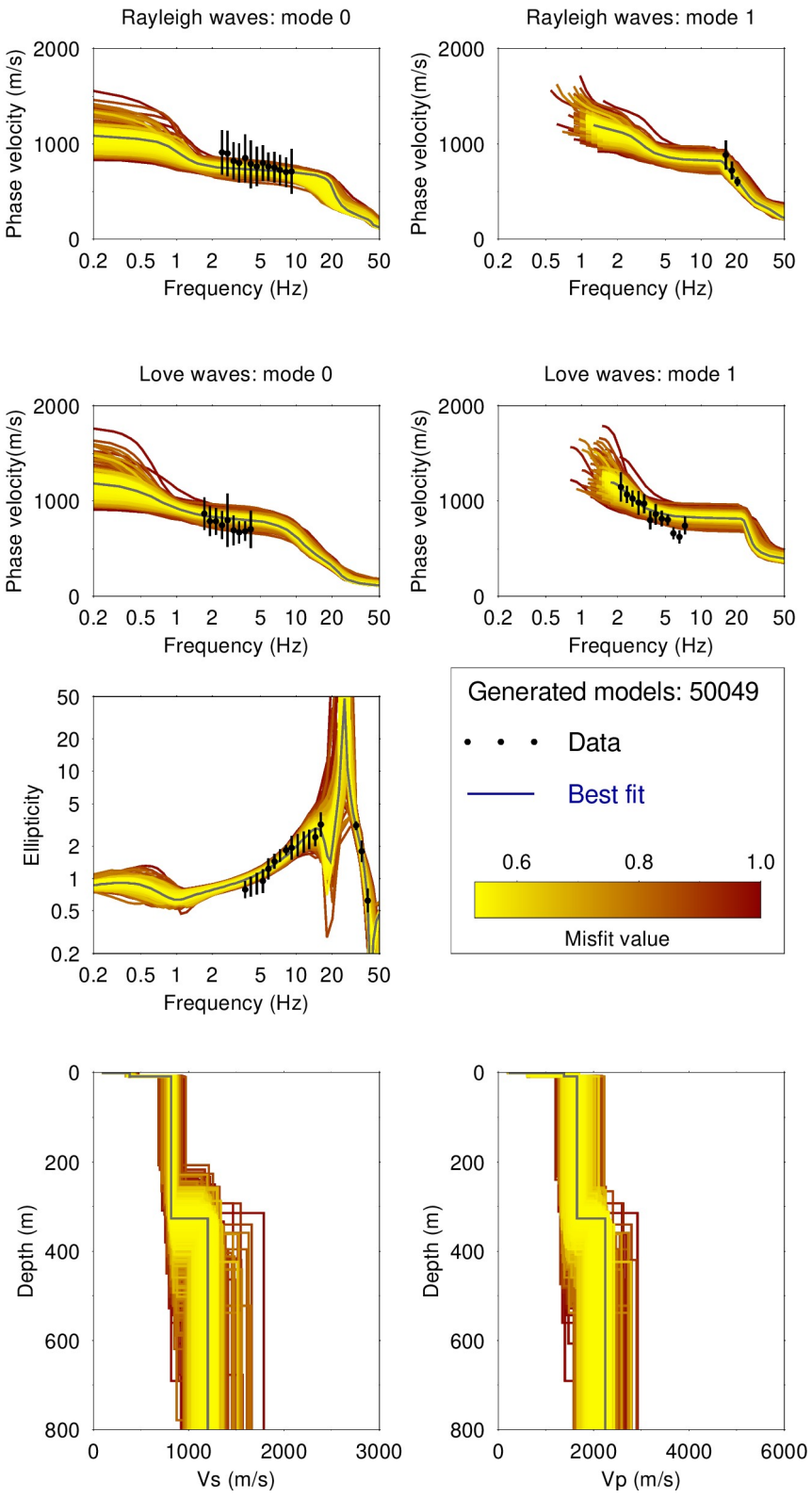

Figure 12: Inversion results using a 3LOH parametrization. The different models are shown in a color according to the misfit value, where the best model is shown in continuous gray color and the black dots indicate the data points that contribute to the inversion.

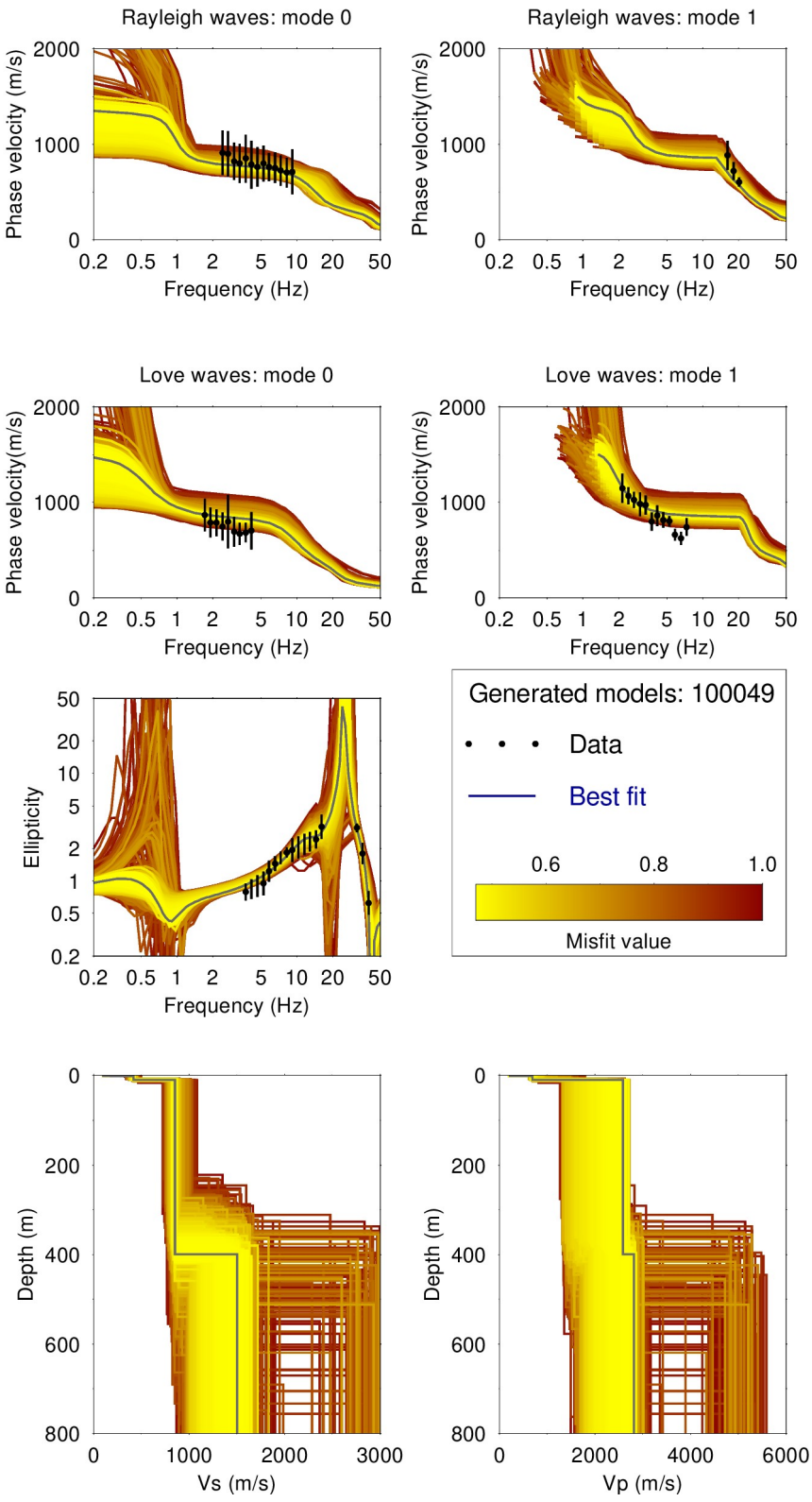

Figure 13: Inversion results using a 4LOH parametrization. The different models are shown in a color according to the misfit value, where the best model is shown in continuous gray color and the black dots indicate the data points that contribute to the inversion.

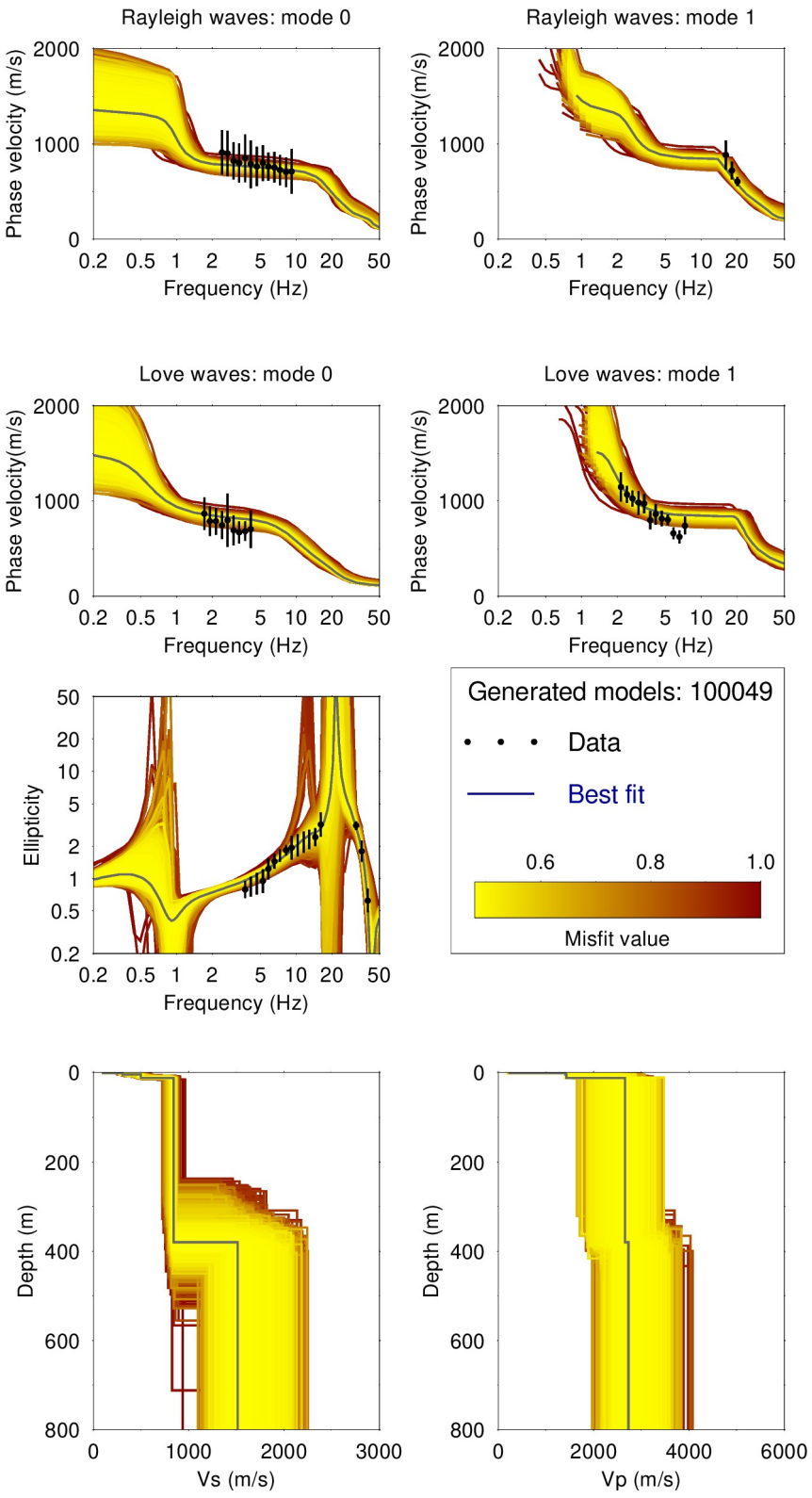

Figure 14: Inversion results using a 5LOH parametrization. The different models are shown in a color according to the misfit value, where the best model is shown in continuous gray color and the black dots indicate the data points that contribute to the inversion.

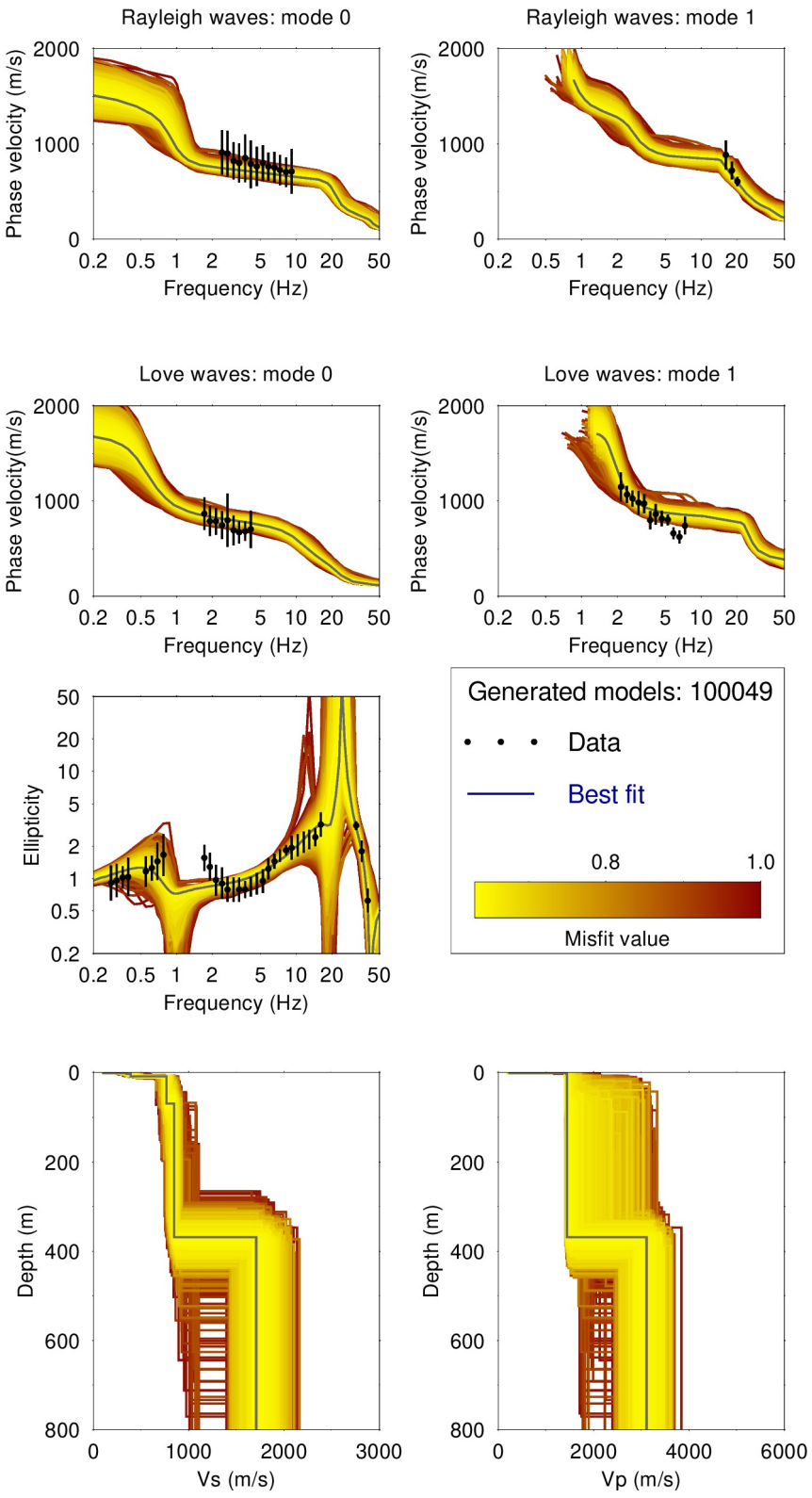

Figure 15: Inversion results using a 6LOH parametrization. The different models are shown in a color according to the misfit value, where the best model is shown in continuous gray color and the black dots indicate the data points that contribute to the inversion.

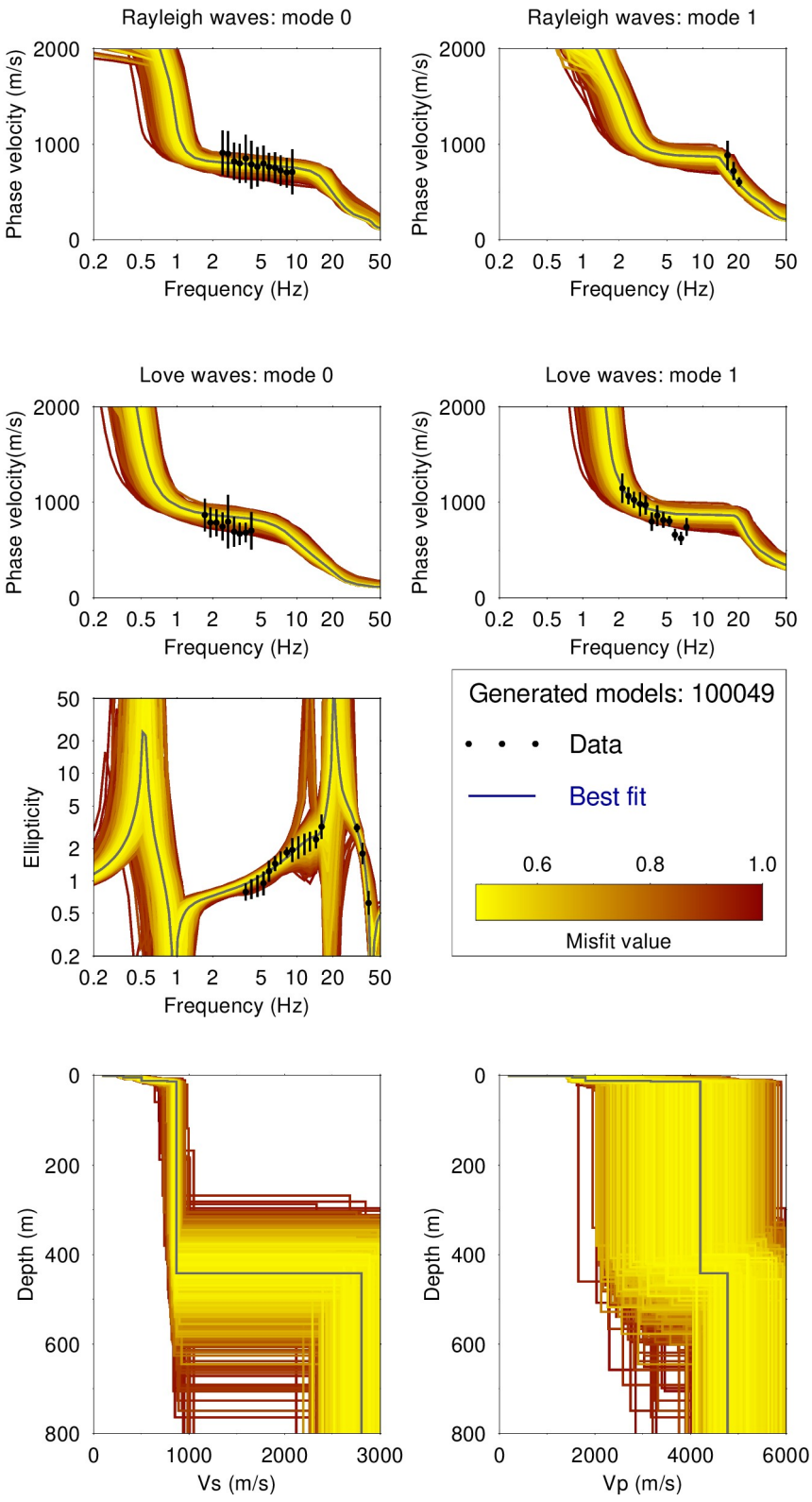

Figure 16: Inversion results using a 7LOH parametrization. The different models are shown in a color according to the misfit value, where the best model is shown in continuous gray color and the black dots indicate the data points that contribute to the inversion.

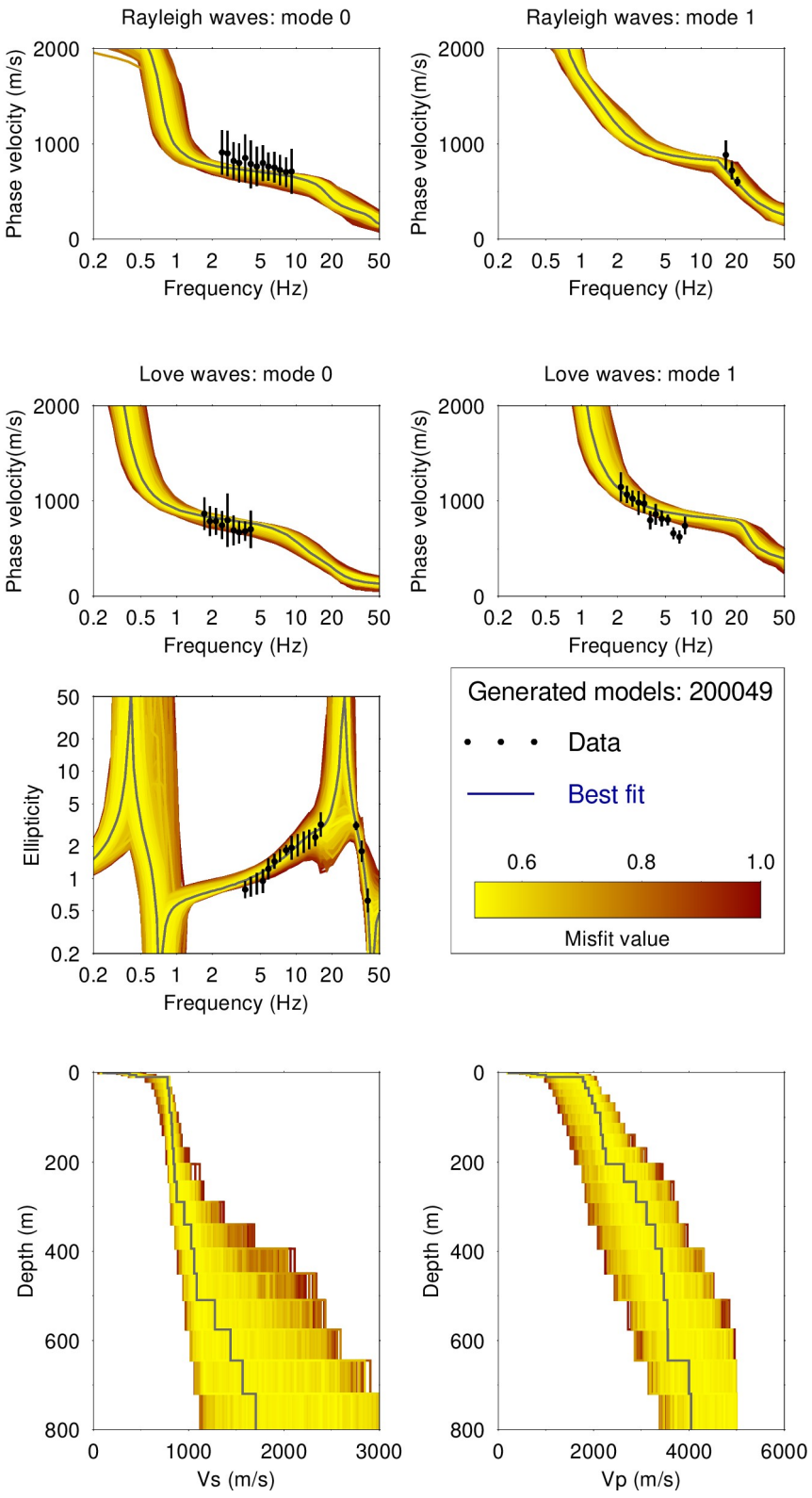

Figure 17: Inversion results using a FixedLayer thickness parametrization. The different models are shown in a color according to the misfit value, where the best model is shown in continuous gray color and the black dots indicate the data points that contribute to the inversion.

6.3 Inversion summary

The best models from the inversions using different parametrizations (3LOH, 4LOH, 5LOH, 6LOH, 7LOH, and FixedLayer) are shown in Figure 18.
The misfit values from the combined inversion vary between 0.47 and 0.54. A comparison of the S- and P-wave velocity profiles indicates that there are mainly three discontinuities around 1, 10, and 400 m. The average V_{S30} from the five (excluding the 3LOH model) best models in the surface wave inversion is 525 $\pm$ 2 m/s. This V_{S30} value corresponds to ground type B in both EC8 (European standard) and SIA261 (Swiss standard).

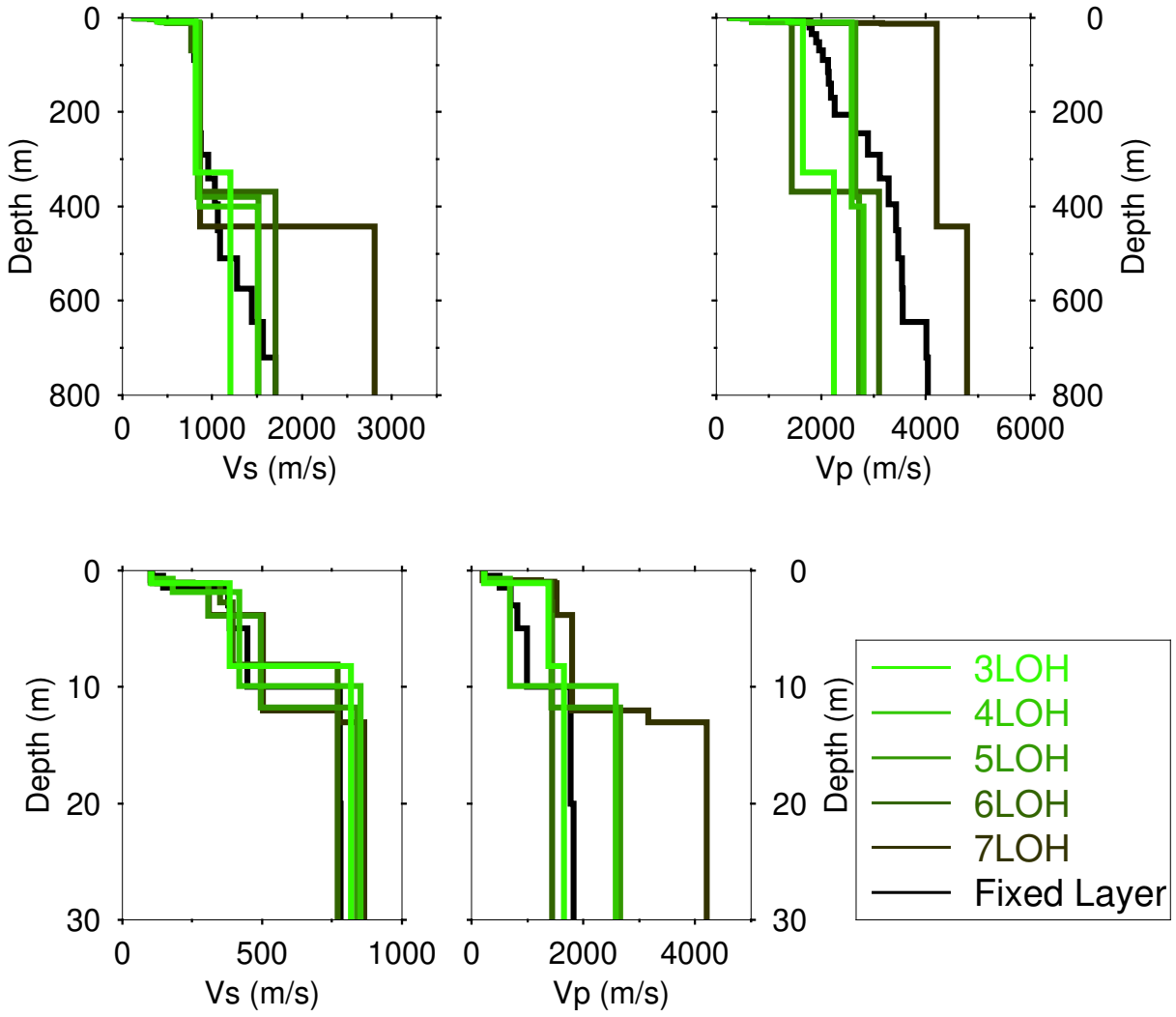

Figure 18: Overview of the best models for the different parameterizations. Top: S-wave (left) and P-wave (right) velocity profiles. Bottom: Zoom on the superficial 30 meters.

6.4 Site amplification

Starting from the best models presented in Figure 18, the theoretical site amplification function is computed and compared with the empirical site amplification function of the station SGWS. The amplification is further calibrated by the one for the Swiss reference profile. The site amplification function is estimated following Edwards et al. (2013). The comparison is shown in Figure 19.
The overall shape of the empirical and theoretical amplification functions agree well in amplitude for the frequency between about 1.7 and 4 Hz.

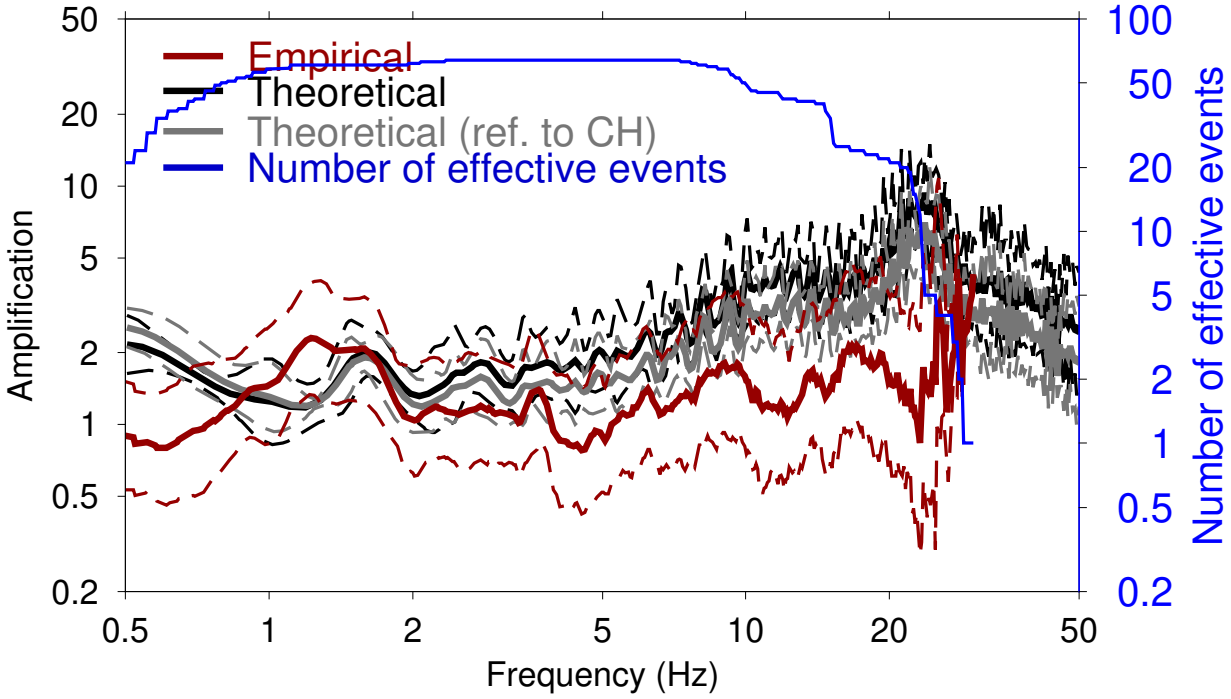

Figure 19: Comparison between the site amplification estimated for the best models from the inversions and the empirical amplification for station SGWS. In addition, the amplification function referenced to the Swiss reference profile and the full H/V spectral ratio curves are plotted.

6.5 Quarter-wavelength representation

The quarter wavelength representation for the joint inversion of ellipticity and dispersion curves is presented in Figure 20.

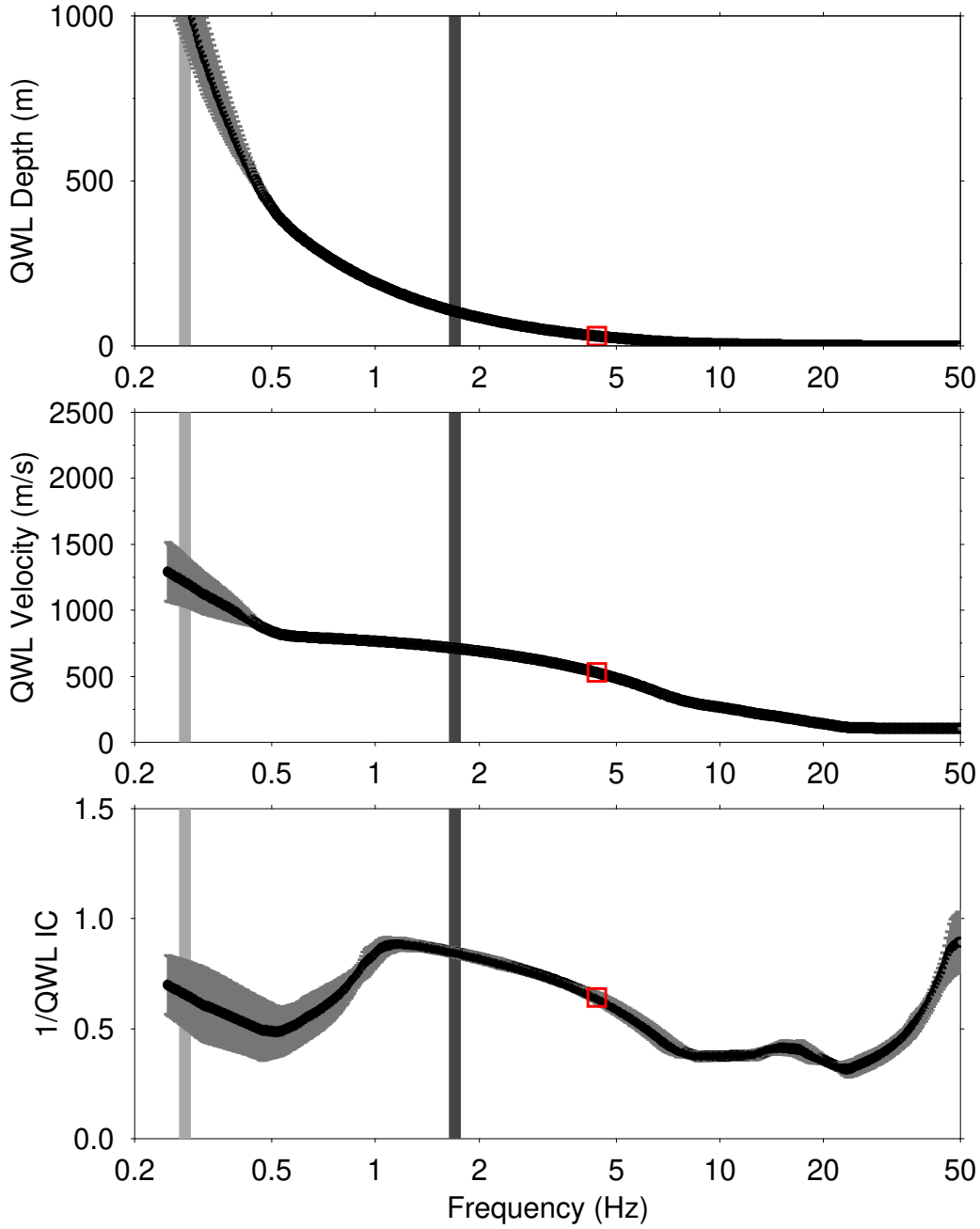

Figure 20: Quarter-wavelength representation for the best models of the inversions. The light and dark gray vertical bars indicate the minimum frequencies for the ellipticity and phase velocities, respectively, used in the inversion process. The solid black line uses all models of Figure 18.

7 Joint inversion of full H/V and phase velocity dispersion curves

7.1 Parametrization

Here also, the inversion assumes a layered earth structure. Three, four, five, six and seven layers over half-space were used. No parameter space with fixed depths was considered.

7.2 Results

Figures 21-25 show the full-HV inversion results. We summarize and interpret the best profiles from the inversion in Figure 26. Table 2 gives a summary of the minimum misfit values achieved in each case during the inversion process.

Table 2: Minimum misfit values for different parametrizations.

Parametrization	Minimum misfit
3 LOH	0.449
4 LOH	0.445
5 LOH	0.456
6 LOH	0.467
7 LOH	0.489

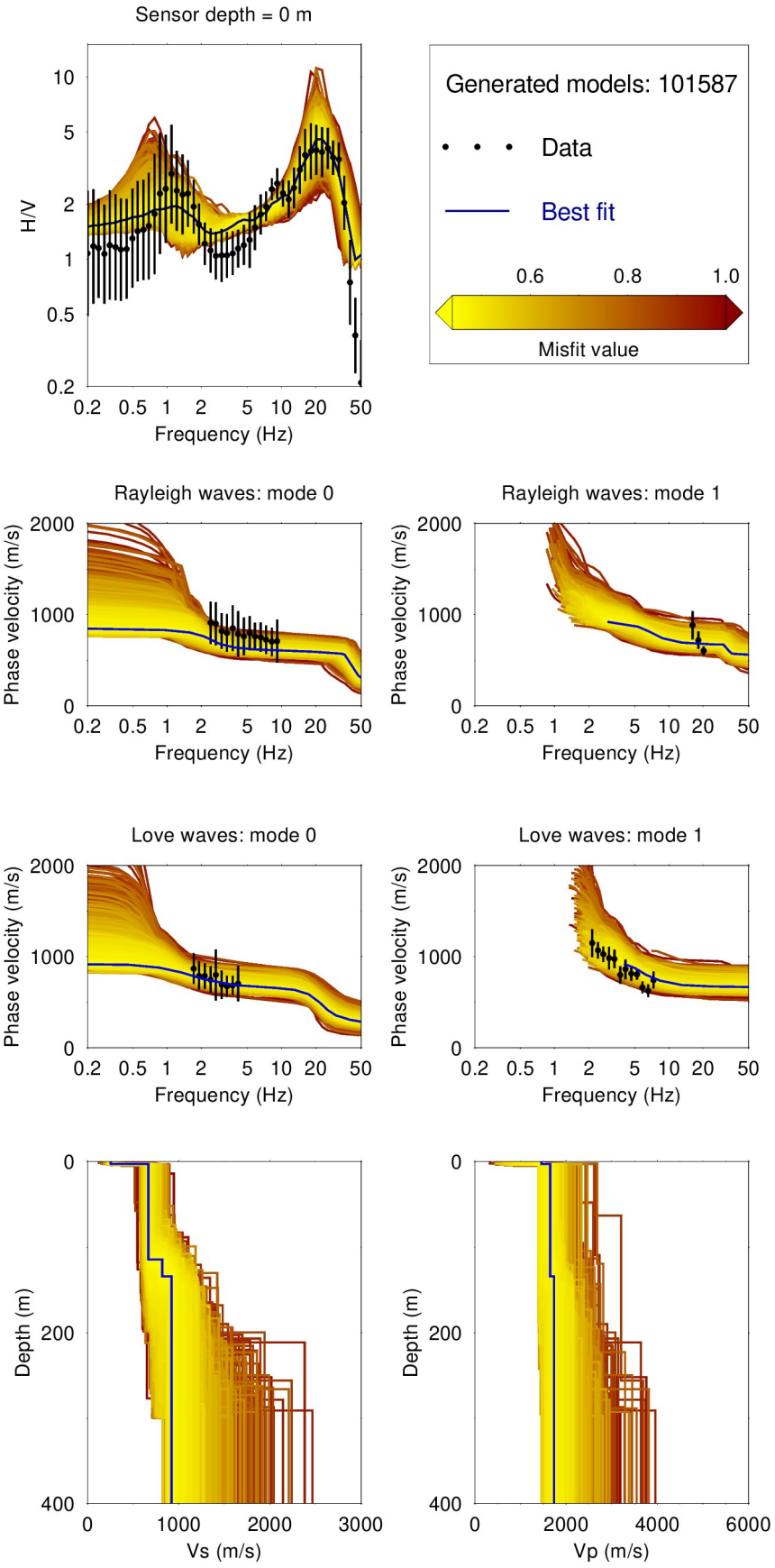

Figure 21: Full-hv-inv results using a 3LOH parametrization. The different models are shown in a color according to the misfit value, where the best model is shown in continuous blue color and the black dots indicate the data points that contribute to the inversion.

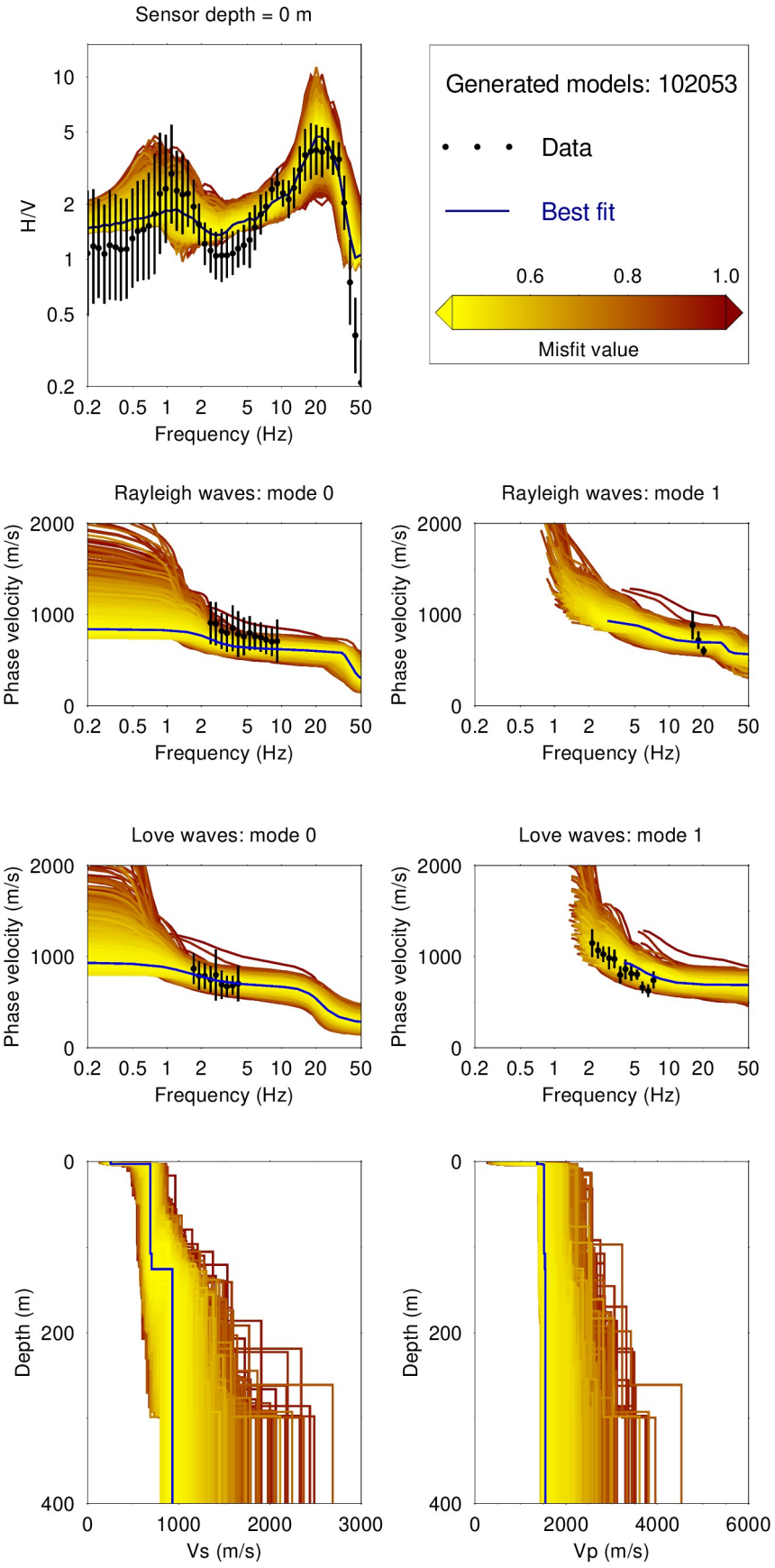

Figure 22: Full-hv-inv results using a 4LOH parametrization. The different models are shown in a color according to the misfit value, where the best model is shown in continuous blue line and the black dots indicate the data points that contribute to the inversion.

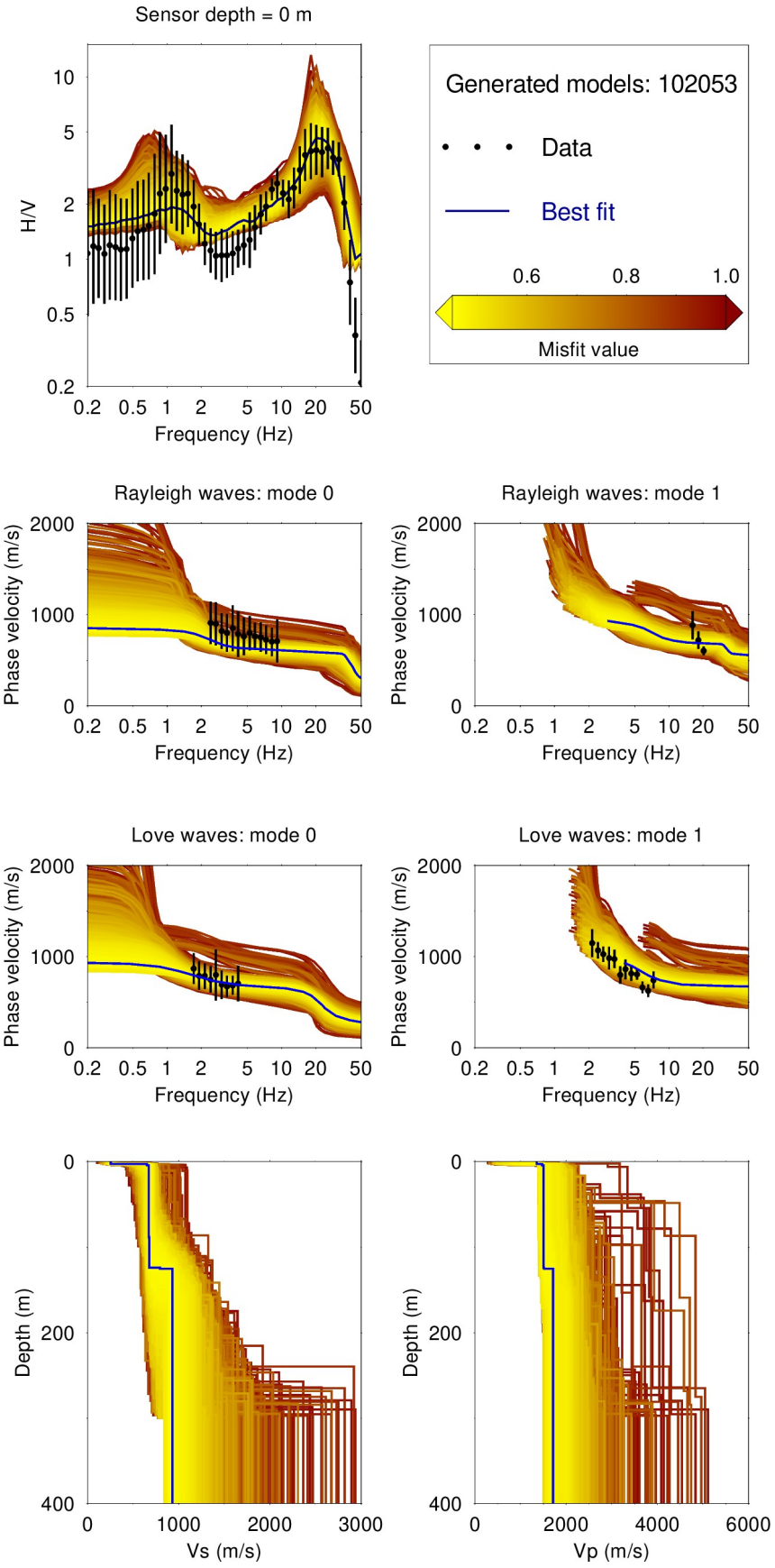

Figure 23: Full-hv-inv results using a 5LOH parametrization. The different models are shown in a color according to the misfit value, where the best model is shown in continuous blue line and the black dots indicate the data points that contribute to the inversion.

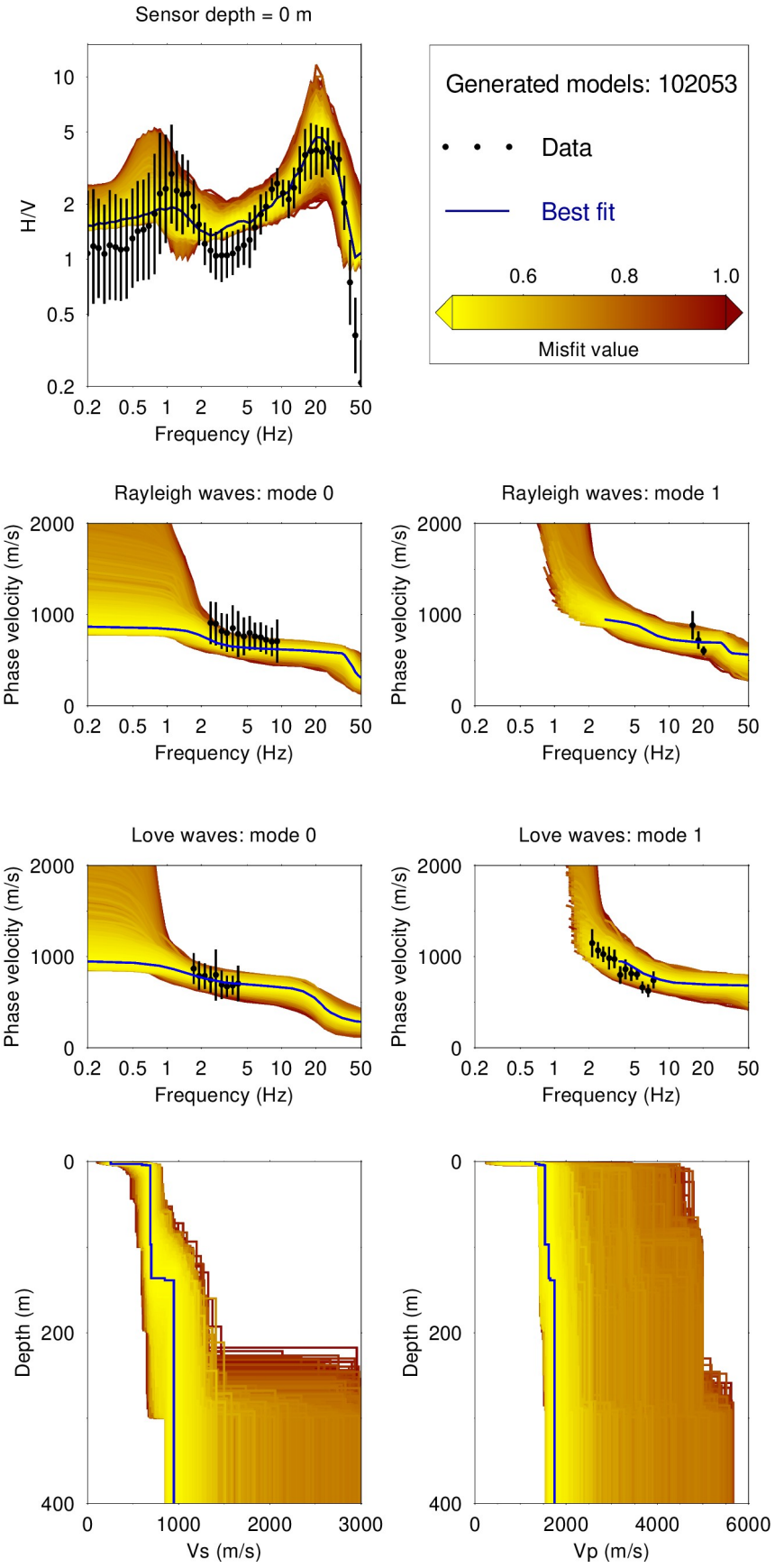

Figure 24: Full-hv-inv results using a 6LOH parametrization. The different models are shown in a color according to the misfit value, where the best model is shown in continuous blue line and the black dots indicate the data points that contribute to the inversion.

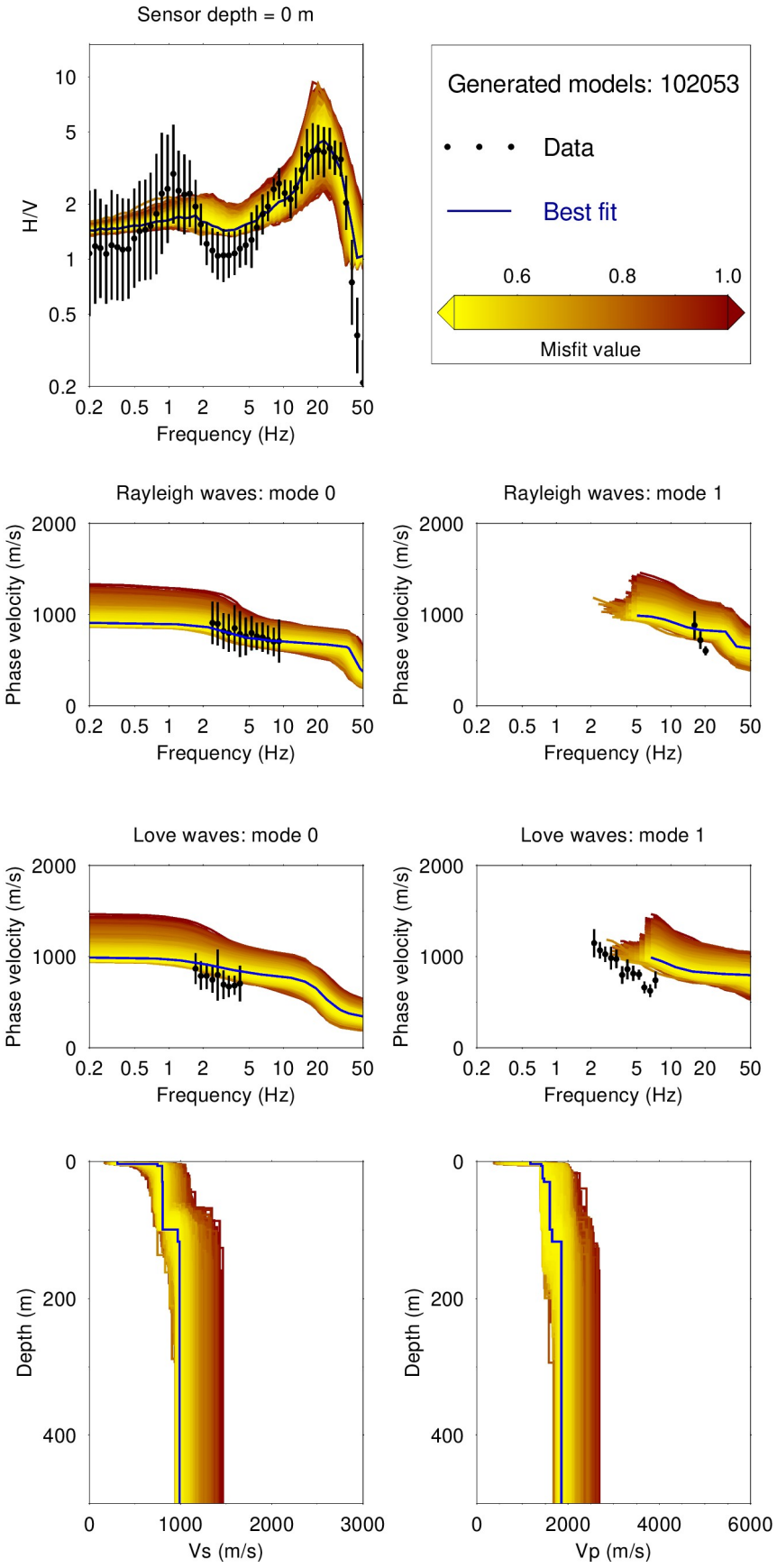

Figure 25: Full-hv-inv results using a 7LOH parametrization. The different models are shown in a color according to the misfit value, where the best model is shown in continuous blue line and the black dots indicate the data points that contribute to the inversion.

7.3 Inversion summary

The best models from the inversions using different parametrizations (3LOH, 4LOH, 5LOH, 6LOH, and 7LOH) are shown in Figure 26.

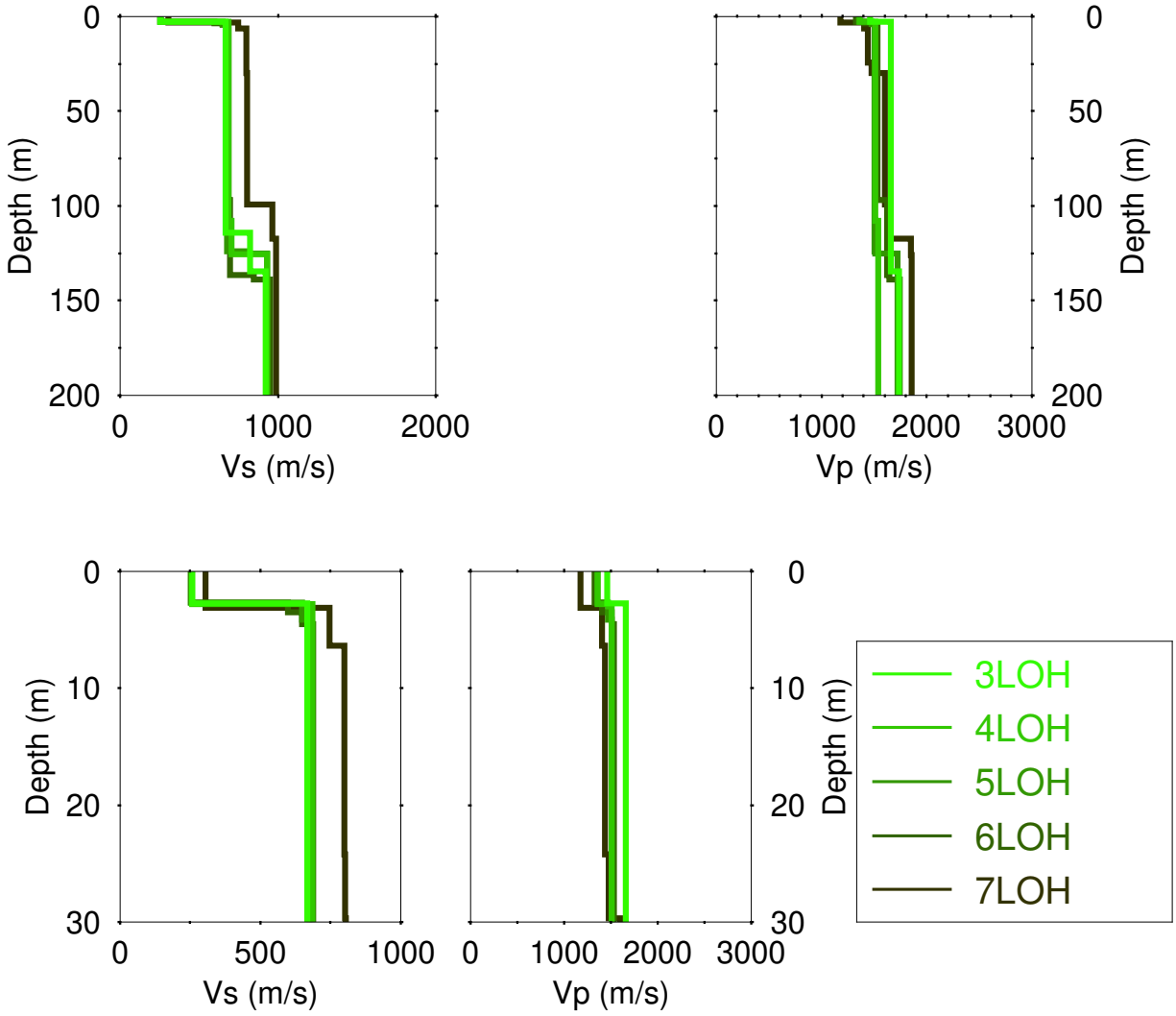

Figure 26: Overview of the best models for the different parameterizations. Top: S-wave (left) and P-wave (right) velocity profiles. Bottom: Zoom on the superficial 30 meters.

The misfit values from the combined inversion vary between 0.44 and 0.49. The average V_{S30} value is 588 ± 2 m/s. This V_{S30} indicates a ground type B in EC8 (European standard) and in SIA261 (Swiss standard).

7.4 Site amplification

Starting from the models presented in Figure 26, excluding the 7LOH best model where no good fit of the Love wave DC curves is observed, the theoretical site amplification function is also computed and compared with the empirical site amplification function from earthquake observations at the station SGWS. Here also, the site amplification function is estimated following Edwards et al. (2013). The comparison is shown in Figure 27.
The curves show good agreement between the 1D SH-wave transfer function and the empirical amplification function on a broad frequency range.

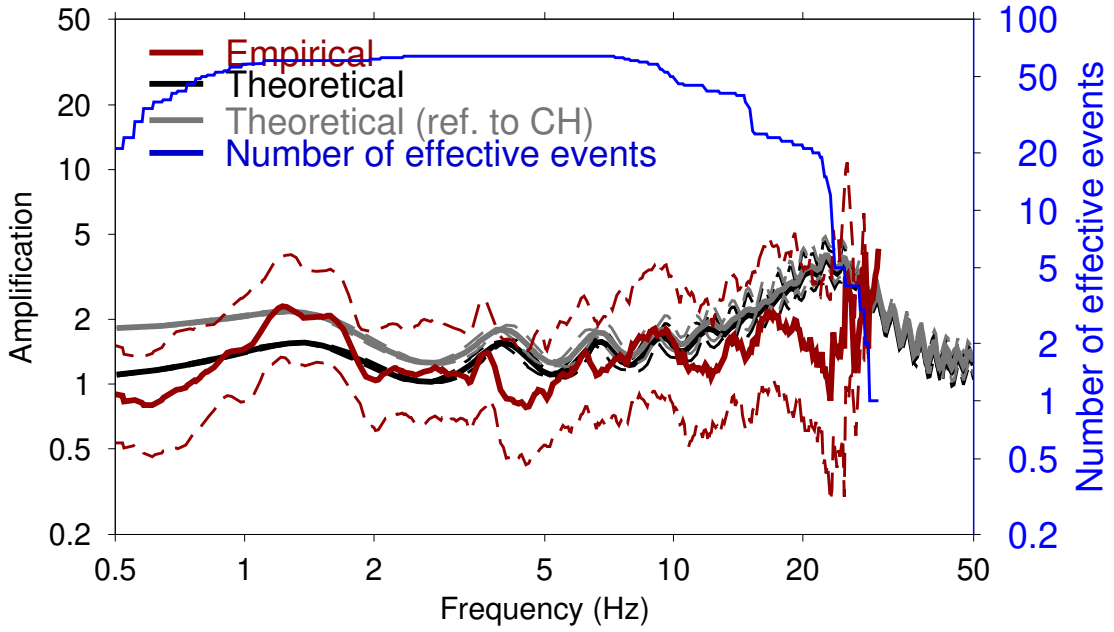

Figure 27: Comparison between the site amplification estimated for the best models from the inversions and the empirical amplification for station SGWS.

7.5 Quarter-wavelength representation

The quarter wavelength representation for the joint inversion of full-HV and dispersion curves is presented in Figure 28.

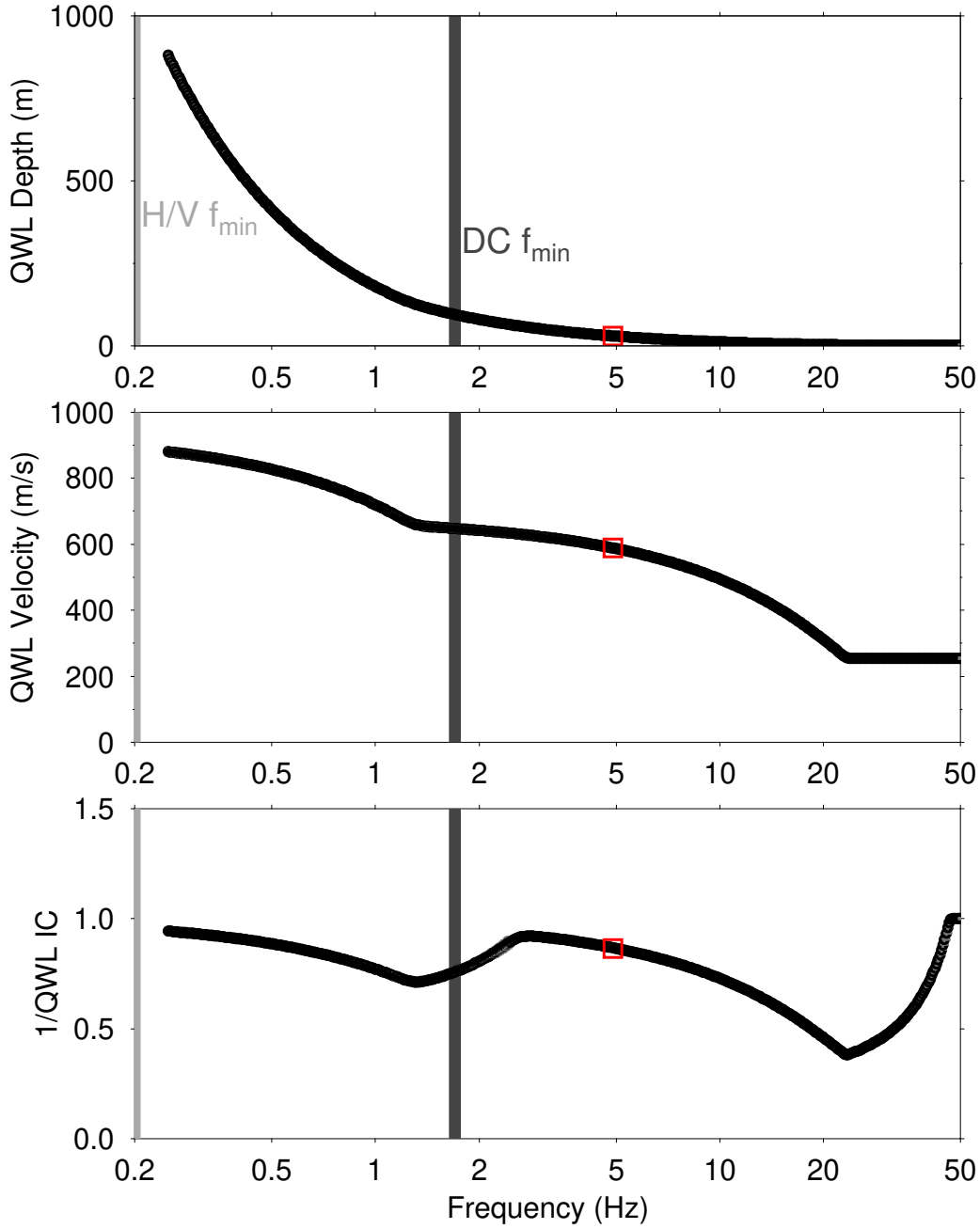

Figure 28: Quarter-wavelength representation for the best models of the inversions. The light and dark gray vertical bars indicate the minimum frequencies for the ellipticity and phase velocities, respectively, used in the inversion process. The solid black line uses the models of Figure 26.

8 Summary of the two inversions

Table 3 gives the summary of the engineering parameters from the two inversions.

Table 3: Comparison of the site parameters from the two inversions.

Engineering parameters and site classification	Ell. + DC inversion	full-hv-inv
V_{S30}	525 ± 2 m/s	588 ± 2 m/s
f_0	1.1 Hz	
Bedrock depth (m)	400	125
z_{800} Depth to engineering bedrock (Depth to shallowest layer exceeding $V_S = 800m/s$)	N/A	N/A
Soil class according to EC8	B	B
Soil class according to SIA	B	B

9 Conclusion

A passive seismic survey was carried out at the strong motion station SGWS at Grindelwald (BE) to characterize the local subsurface. The dispersion curves for Love and Rayleigh waves were estimated over a frequency band ranging from 1.7 Hz to 20.3 Hz. Two frequency peaks were measured for the H/V spectral ratio and ellipticity at around 1.1 and 25.7 Hz, where the peak at 25.7 Hz is dominant. Around these peak frequencies, the energy on the vertical component is vanishing. The array methods used were complementary in selecting the appropriate dispersion curve branch for the fundamental mode Rayleigh waves. Two inversion were used: the first inversion used dinver to invert the ellipticity and dispersion curves as targets and the second inversion used full-hv-inv to invert the H/V spectral ratio and the dispersion curves. The left and right flanks of the ellipticity curves around the peak frequency at 25.7 Hz were used in the inversion and the peak at 1.1 Hz was used as an additional constraint. The results from dinver (ellipticity and peak frequency and dispersion curves) indicate a bedrock depth at 400 m and a V_{S30} value of 525 ± 2. Full-hv-inv (H/V and dispersion curves) inversion estimated the bedrock depth at about 125 m and a V_{S30} value of 588 ± 2 m/s. For these V_{S30} values, the ground is classified as ground type B in EC8 (European standard) and in SIA261 (Swiss standard). From the best velocity profiles obtained from the two inversions, the 1D SH-wave amplification were calculated and the results were compared with the emnpirical spectral modelling curves obtained using earthquake data. A good comparison between the theoretical and empirical amplification curves is obtained for the best profile estimated from full-hv-inv.

10 Acknowledgments

Dario Chieppa and Manuel Studer helped during the array measurements.

References

Aki, K., 1957. Space and time spectra of stationary stochastic waves, with special reference to microtremors., *Bull. Earthq. Res. Inst.*, **35**, 415–456.

Bettig, B., Bard, P. Y., Scherbaum, F., Riepl, J., Cotton, F., Cornou, C., & Hatzfeld, D., 2001. Analysis of dense array noise measurements using the modified spatial auto-correlation, *Boll. Geof. Teor. Appl.*, **42**, 281–304.

Burjánek, J., Gassner-Stamm, G., Poggi, V., Moore, J. R., & Fäh, D., 2010. Ambient vibration analysis of an unstable mountain slope, *Geophysical Journal International*, **180**(2), 820–828.

Burjánek, J., Moore, J. R., Yugsi Molina, F. X., & Fäh, D., 2012. Instrumental evidence of normal mode rock slope vibration, *Geophysical Journal International*, **188**(2), 559–569.

Edwards, B., Michel, C., Poggi, V., & Fäh, D., 2013. Determination of Site Amplification from Regional Seismicity: Application to the Swiss National Seismic Networks, *Seismological Research Letters*, **84**(4), 611–621.

Fäh, D., Kind, F., & Giardini, D., 2001. A theoretical investigation of average H/V ratios, *Geophysical Journal International*, **145**(2), 535–549.

Fäh, D., Wathelet, M., Kristekova, M., Havenith, H.-B., Endrun, B., V., G. S., Poggi, Burjanek, J., & Cornou, C., 2009. Using ellipticity information for site characterisation using ellipticity information for site characterisation, *Technical report, NERIES JRA4*.

Hobiger, M., Bard, P.-Y., Cornou, C., & Le Bihan, N., 2009. Single station determination of Rayleigh wave ellipticity by using the random decrement technique (RayDec), *Geophysical Research Letters*, **36**(14), n/a–n/a, L14303.

Hobiger, M., Cornou, C., Wathelet, M., Giulio, G. D., Knapmeyer-Endrun, B., Renalier, F., Bard, P.-Y., Savvaidis, A., Hailemikael, S., Le, B. N., Ohrnberger, M., & Theodoulidis, N., 2013. Ground structure imaging by inversions of rayleigh wave ellipticity: sensitivity analysis and application to european strong-motion sites, *Geophysical Journal International*, **192**(1), 207–229.

Lontsi, A., Ohrnberger, M., & Krüger, F., 2016a. Shear wave velocity profile estimation by integrated analysis of active and passive seismic data from small aperture arrays, *Journal of Applied Geophysics*, **130**, 37 – 52.

Lontsi, A. M., Ohrnberger, M., Krüger, F., & Sánchez-Sesma, F. J., 2016b. Combining surface wave phase velocity dispersion curves and full microtremor horizontal-to-vertical spectral ratio for subsurface sedimentary site characterization, *Interpretation*, **4**(4).

Maranò, S., Reller, C., Loeliger, H.-A., & Fäh, D., 2012. Seismic waves estimation and wavefield decomposition: application to ambient vibrations, *Geophysical Journal International*, **191**(1), 175–188.

Poggi, V. & Fäh, D., 2010. Estimating rayleigh wave particle motion from three-component array analysis of ambient vibrations, *Geophysical Journal International*, **180**(1), 251–267.

Sambridge, M., 1999. Geophysical inversion with a neighbourhood algorithm—i. searching a parameter space, *Geophysical Journal International*, **138**(2), 479–494.

Scherbaum, F., Hinzen, K.-G., & Ohrnberger, M., 2003. Determination of shallow shear wave velocity profiles in the Cologne, Germany area using ambient vibrations, *Geophysical Journal International*, **152**(3), 597–612.

Wathelet, M., 2008. An improved neighborhood algorithm: Parameter conditions and dynamic scaling, *Geophysical Research Letters*, **35**(9).